Temperature and intrinsic Ca^{2+} reshape TRPM4 pharmacology

Jinhong Hu[1], Sofia Ievleva[1], Sung Jin Park[1], Junuk Lee[1], Jennifer Cheng[1], Garrett O'Dea[1], Jiangnan Sheng[1], Juan Du[#1,2,3] & Wei Lü[#1,2,3]

1. Department of Molecular Biosciences, Northwestern University, Evanston, IL, USA
2. Department of Pharmacology, Feinberg School of Medicine, Northwestern University, Chicago, IL, USA
3. Chemistry of Life Processes Institute, Northwestern University, Evanston, IL, USA

#CORRESPONDING AUTHOR

Correspondence and requests for materials should be addressed to J. D. (email: juan.du@northwestern.edu) TEL: (847) 467-6719, or W. L. (email: wei.lu@northwestern.edu). TEL: (847) 491-5440

Abstract

Proteins operate in dynamic environments where ions, lipids, and temperature collectively define their properties, yet most studies rely on simplified conditions that overlook these intrinsic variables. Here, we show two such factors—temperature and Ca^{2+}—profoundly remodel the function and pharmacology of TRPM4, an ion channel implicated in cardiac conduction, immune regulation, cancer, and intestinal fluid homeostasis. At physiological temperature and Ca^{2+}, TPPO—previously considered a selective TRPM5 inhibitor inactive toward TRPM4—potently activates TRPM4, revealing strong synergy among temperature, Ca^{2+}, and ligand binding. In contrast, Necrocide-1, a necroptotic activator targeting the same binding pocket, defies this logic: it opens TRPM4 without Ca^{2+} but is antagonized by Ca^{2+}. Meanwhile, the inhibitors NBA and CBA engage a nearby pocket, locking the channel in a non-conductive pre-open state. Our findings highlight that even rigid binding pockets can exhibit temperature-dependent ligand recognition, revealing hidden pharmacology and informing selective, environment-aware therapeutic strategies.

Introduction

Protein activity is inherently governed by the cellular environment in which it operates. A wide array of factors—including ions, lipids, temperature, pH, and protein–protein interactions—collectively determine how a protein functions in its native context. Yet, because of technical constraints, most biophysical and pharmacological studies have been conducted under simplified conditions, which have yielded foundational insights but often fail to capture the full physiological complexity.

Increasing efforts now aim to bridge this gap by incorporating more native variables—for example, using nanodiscs, liposomes or membrane-derived vesicles to preserve native lipidic environments for membrane proteins[1-4], and purifying proteins from native sources to retain endogenous protein compositions and modifications[5-8]. Despite these advances, one fundamental determinant, temperature, is largely overlooked in mechanistic and pharmacological studies, even though it influences every protein in the human body, where proteins operate at 37°C. Because most in vitro assays are performed at room temperature or lower, therefore, the broad impact of temperature on protein conformation, ligand recognition, efficacy and mechanism remains unexplored, with only a few recent exceptions[9,10].

Alongside temperature, intracellular Ca^{2+} represents another intrinsic physiological variable that exerts pervasive influence on protein behavior. Although not universal, Ca^{2+} acts as a selective yet broad regulator of cellular physiology. It is among the most tightly controlled cellular cofactors, with cytosolic concentrations fluctuating dynamically from tens of nanomolar at rest to low micromolar during signaling, and rising to abnormally high levels under pathological conditions such as ischemia, excitotoxicity, or cancer[11]. Many proteins are directly regulated by Ca^{2+} through dedicated binding sites, while others respond indirectly through Ca^{2+}-dependent signaling cascades. Although the structural and functional roles of Ca^{2+} have been extensively characterized, its impact on protein–ligand interactions—particularly in combination with other intrinsic factors like temperature—has rarely been considered. This represents an important gap in our understanding of how Ca^{2+}-regulated proteins engage ligands under physiological and pathological conditions.

The Ca^{2+}-activated, temperature-sensitive channel Transient Receptor Potential Melastatin 4 (TRPM4) provides an ideal model to investigate how intrinsic physiological factors remodel

70 pharmacology[12-15]. TRPM4 is a non-selective monovalent cation channel whose activation by
71 elevated cytosolic Ca^{2+}—arising from receptor-mediated signaling, Ca^{2+} entry through other
72 channels, or release from intracellular stores—leads to Na^{+} influx and membrane depolarization.
73 This depolarization activates downstream depolarization-dependent mechanisms, including the
74 regulation of voltage-gated ion channels, and thereby modulates diverse downstream processes
75 such as cardiac conduction, insulin secretion, neuronal excitability, immune regulation, and
76 intestinal fluid homeostasis[16-25]. Pathogenic variants have been implicated in Brugada syndrome,
77 a genetic heart rhythm disorder, and other inherited conduction disorders, as well as diverse
78 cancers[26-34]. In this context, TRPM4 antagonists may be therapeutically beneficial in cardiac
79 diseases where excessive TRPM4 activity contributes to pathological depolarization and
80 conduction defects, whereas TRPM4 agonists may be relevant in certain cancers in which
81 TRPM4 is upregulated, where enhanced channel activity has been associated with necrotic cell
82 death pathways. Despite this broad physiological and pathological relevance, TRPM4 has
83 remained largely untargeted by clinical pharmacology, with the single exception of bisacodyl—a
84 widely used drug for chronic constipation—and its active metabolite deacetyl bisacodyl, which
85 we recently identified and characterized as clinically relevant TRPM4 agonists[25].

86 Our previous structural and functional studies revealed that TRPM4 adopts two major
87 conformations, a "cold" and a "warm" state, whose equilibrium is governed jointly by
88 temperature and cytosolic Ca^{2+} concentration[10]. In the cold conformation, Ca^{2+} binds exclusively
89 to an agonist site within the S1–S4 bundle (Ca_{TMD}), giving rise to strongly outwardly rectifying
90 currents. In contrast, in the warm conformation, the intracellular domain undergoes a pronounced
91 rearrangement accompanied by Ca^{2+} binding at an additional intracellular site (Ca_{warm} or Ca_{ICD}),
92 resulting in currents that are less outwardly rectifying and exhibit substantial inward
93 conductance. Together, these findings suggest that biophysical and pharmacological assays
94 performed under room temperature and undefined Ca^{2+} conditions may not accurately capture
95 the channel's behavior under physiological settings.

96 Here, we systematically examine TRPM4 pharmacology under conditions that incorporate
97 both temperature and Ca^{2+}. Through combined cryo-EM and electrophysiology, we reveal that
98 these intrinsic factors profoundly shape ligand recognition, efficacy, and mechanism. Our results
99 identify the S1–S4 domain as a dynamic regulatory hub that integrates environmental and

chemical cues to govern activation and inhibition. More broadly, this work establishes an environment-aware framework for pharmacology, in which incorporating intrinsic variables exposes hidden drug activities and new mechanisms of regulation. For widely expressed proteins like TRPM4, such principles open opportunities to design therapeutics that exploit pathological local conditions—such as abnormally elevated Ca^{2+} or altered thermal states—for selective action in disease, while preserving normal physiological function and minimizing side effects.

Results

Temperature reveals hidden pharmacology of TRPM4

During the cold-to-warm transition of TRPM4, Ca^{2+} and temperature drive major conformational changes in the intracellular domain but only subtle shifts in the transmembrane domain[10]. From these structures, we identified three categories of ligand binding sites that emerge elusively in the warm conformation of the intracellular domain[10]. While this outcome may be anticipated from the magnitude of ICD rearrangement, it nevertheless raises two central questions: whether drug screening performed exclusively at room temperature may have overlooked active compounds, and whether temperature-dependent ligand recognition is confined to regions undergoing large conformational change (such as the intracellular domain) or extends to regions with more modest movements (such as the transmembrane domain).

To address these questions, we examined several previously reported TRPM4 ligands, as well as compounds considered inactive toward TRPM4. We focused on hydrophobic ligands predicted to interact with the transmembrane domain, including triphenylphosphine oxide (TPPO), necrocide-1 (NC1), and the anthranilic acid derivatives CBA (4-chloro-2-[2-(2-chloro-phenoxy)-acetylamino]-benzoic acid) and NBA (4-chloro-2-(2-(naphthalene-1-yloxy) acetamido) benzoic acid). TPPO, originally identified as a selective TRPM5 inhibitor with an IC_{50} of 12 μM, has been found inactive on TRPM4 when tested using fluorescence-based membrane potential assays[35]. NC1 was recently characterized as a TRPM4 activator that promotes Na^{+} influx and triggers necrotic cell death[36], suggesting therapeutic potential in cancer. NBA and CBA represent the best-characterized TRPM4 inhibitors to date with IC_{50} in the sub-micromolar range[37]. Importantly, all prior functional and structural studies were conducted at room temperature or lower.

Using patch-clamp electrophysiology, we tested these compounds at both room temperature and 37°C. Under previously reported assay conditions—room temperature with either zero free intracellular Ca^{2+} or basal free intracellular Ca^{2+} (100 nM), we reproduced established results: 50 μM TPPO showed negligible activity on TRPM4—comparable to the control group, where basal Ca^{2+} alone is insufficient to drive channel activation (Fig. 1a,b; Extended Data Fig. 1a,b); NC1 activated the channel, eliciting largely linear, voltage-independent currents (Fig. 2a,b); and NBA and CBA produced robust inhibition of Ca^{2+}-induced TRPM4 current (Extended Data Fig. 2a). Strikingly, elevating the temperature to 37 °C revealed a hidden pharmacological behavior. While NC1, NBA, and CBA retained their room-temperature profiles (Fig. 2d,e; Extended Data Fig. 2a), TPPO displayed a completely different response—robustly activating TRPM4 currents (Fig. 1e; Extended Data Fig. 1e). These observations highlight a critical gap in conventional pharmacological screening: assays performed under non-physiological conditions may both overlook potential active compounds and misclassify ligand selectivity.

Ca^{2+} as a key determinant of agonist recognition and potency in TRPM4

Ca^{2+} is the only known endogenous agonist of TRPM4, and together with temperature, drives the transition between its cold to warm conformations[10]. Building on our findings that temperature reshapes TRPM4 pharmacology (Fig. 1e), we next explored whether Ca^{2+} modulates the binding and potency of the exogenous activators TPPO and NC1.

Under Ca^{2+}-free conditions achieved by EGTA buffering, 50 uM TPPO produced negligible activation of TRPM4 (Fig. 1d; Extended Data Fig. 1d), whereas adding 100 nM free intracellular Ca^{2+} enabled robust activation (Fig. 1e, red traces; Extended Data Fig. 1e). Thus, even basal Ca^{2+} concentrations—although insufficient to open the channel alone (Fig. 1e, black trace; Extended Data Fig. 1e)—markedly enhance TPPO-induced TRPM4 activation. To quantify this apparent synergy, we determined TPPO dose-response relationships. Physiological temperature increased TPPO potency by ~14-fold under basal Ca^{2+} (Fig. 1g,h; Extended Data Fig. 1g,h), while basal Ca^{2+} increased TPPO potency by ~6-fold at 37 °C (Fig. 1g,i; Extended Data Fig. 1g,i). In the absence of both Ca^{2+} and physiological temperature, TPPO activated TRPM4 only weakly at submillimolar concentrations and failed to reach saturation even at millimolar levels. When intracellular Ca^{2+} reach activating level (1 μM), the effect of TPPO is largely—though not completely—masked. Under these conditions, the current recorded in the presence of TPPO

159 appeared relatively linear and closely resembled that observed in the absence of TPPO, a
160 phenotype we previously reported for TRPM4 activated by 1 μM Ca^{2+} at 37 °C[10], aside from
161 minor differences that may reflect a combined contribution of TPPO and Ca^{2+}. Together, these
162 observations are consistent with TPPO and Ca^{2+} acting through a shared activation pathway, with
163 Ca^{2+} becoming the dominant determinant of the channel behavior at high concentrations (Fig.
164 1c,f; Extended Data Fig 1c,f).

165 Together, these data demonstrate that physiological context is essential for TPPO efficacy,
166 revealing a three-way synergy between temperature, Ca^{2+}, and ligand binding. This context
167 dependence overturns the view that TPPO is inactive toward TRPM4, revealing instead that it
168 potently activates the channel—opposite to its inhibitory action on the closely related TRPM5[35].
169 This finding underscores how ligand behavior can be fundamentally mischaracterized when
170 assays are performed under non-physiological conditions.

171 We next examined whether Ca^{2+} influences NC1, previously reported as the first Ca^{2+}-
172 independent agonist of TRPM4[36]. Under Ca^{2+}-free and 100 nM Ca^{2+} conditions, NC1 evoked
173 nearly identical currents with linear current-voltage relationships distinct from Ca^{2+}-activated
174 currents, confirming that NC1 can activate TRPM4 independently with an EC_{50} in the
175 submicromolar range (Fig. 2a,b,d,e,g,h; Extended Data Fig. 3a). However, at 1 μM Ca^{2+}, a
176 physiologically relevant level during cellular stress that robustly activates TRPM4, the response
177 changed dramatically, becoming strongly outwardly rectified (Fig. 2c,f)—a hallmark of
178 canonical Ca^{2+}-mediated activation[14]. This striking reversal suggests that NC1 is not simply
179 Ca^{2+}-independent: once Ca^{2+} reaches activating levels, its action dominates, functionally
180 masking NC1-mediated gating even at saturating NC1 concentrations (Fig. 2i). Thus, rather than
181 bypassing the Ca^{2+} requirement, NC1 displays a biphasic Ca^{2+} dependence: permissive at basal
182 Ca^{2+}, yet exhibiting little to no additional effect at higher Ca^{2+} concentrations. This behavior is
183 most consistent with NC1 becoming functionally masked or antagonized at elevated Ca^{2+}, either
184 through reduced/abolished NC1 binding due to Ca^{2+}-dependent competition, or through allosteric
185 coupling between NC1- and Ca^{2+}-binding sites in scenarios where co-binding occurs. Which
186 mechanism is more likely is discussed further in the section "Mechanistic basis for Ca^{2+}-
187 dependent gating reversal of NC1".

188 Taken together, these results reveal distinct modes of Ca^{2+}-agonist interplay in TRPM4.
189 TPPO requires basal Ca^{2+} (and temperature) to act effectively on the channel, whereas NC1
190 functions independent of Ca^{2+} at rest but loses efficacy once Ca^{2+} rises to stimulatory levels. This
191 contrast illustrates how the same intrinsic cofactor can differentially tune ligand action through
192 cooperative or antagonistic coupling. More broadly, they reinforce the importance of evaluating
193 ion channel pharmacology under physiological conditions, as environmental context can
194 fundamentally alter both efficacy and apparent selectivity.

195 **Structural basis of the three-way synergy between TPPO, temperature and Ca^{2+}**

196 To elucidate how temperature and Ca^{2+} shape TPPO activation of TRPM4, we determined cryo-
197 EM structures of the channel in the presence of TPPO at 18 °C and 37 °C, under both Ca^{2+}-free
198 and Ca^{2+}-saturated conditions. All the structures were resolved to high quality at ~2.5–2.9 Å
199 resolutions, allowing unambiguous identification of ligand binding sites (Extended Data Figs. 4–
200 5; Supplementary Fig. 1; Supplementary Data Table 1).

201 In the consensus map of the Ca^{2+}/TPPO–TRPM4–37°C dataset, we observed a prominent
202 tripod-shaped density in the S1–S4 domain of each protomer. This feature closely matches the
203 shape of TPPO, and sits immediately above the Ca_{TMD} site (Fig. 3a). We therefore designated this
204 pocket as the S1–$S4_{Upper}$ site. This site spatially overlaps with the deacetyl bisacodyl binding
205 pocket we identified previously[25]. Subunit-level classification revealed that where warm and cold
206 conformations coexist in this dataset, with the warm state predominating (Extended Data Fig. 4).
207 The ligand density is markedly stronger in the warm state, whereas a weaker yet still discernible
208 density exists in the cold state (Fig. 3d; this minor cold state is discussed at the end of this
209 section). Within this pocket, TPPO occupies a hydrophobic cavity and forms a critical polar
210 interaction between its phosphoryl moiety and R1072 on the TRP helix (Fig. 3d, left panel). To
211 validate this assignment, we mutated key coordinating residues to alanine and performed
212 electrophysiological recording. Most mutations impaired Ca^{2+}-dependent activation, likely by
213 disrupting the integrity of the adjacent Ca_{TMD} site, making it impossible to unambiguously isolate
214 their effects on TPPO, as TPPO requires Ca_{TMD} to manifest its activity (Extended Data Fig. 1j).
215 In contrast, R1072A preserved Ca^{2+}-evoked gating yet abolished TPPO-dependent activation,
216 thereby confirming the functional relevance of the TPPO binding site (Extended Data Fig. 1k).

In the Ca^{2+}-bound cold conformation from the Ca^{2+}/TPPO–TRPM4–18°C dataset, only a faint and incomplete signal was discernible at the S1–$S4_{Upper}$ site at very low contour levels (Fig. 3b). The density formed a triangular outline reminiscent of TPPO but was markedly smaller than the full ligand, consistent with partial or unstable occupancy. In the Ca^{2+}-free cold conformation from the EGTA/TPPO–TRPM4–37°C dataset, this feature disappeared entirely, with no trace of TPPO density detectable (Fig. 3c).

Thus, TPPO binding exhibits a clear dependence on the cold–warm conformational equilibrium of TRPM4, a transition that is cooperatively governed by temperature and Ca^{2+} (ref[10]). This structural observation coincides with our electrophysiological finding that TPPO, temperature, and Ca^{2+} act in three-way synergy to promote channel activation (Fig. 1a,b,d,e). Together, these results suggest that TPPO efficacy is tightly coupled to the conformational landscape defined by these two intrinsic modulators.

To dissect the mechanism underlying this coupling, we compared the Ca^{2+}-free cold and Ca^{2+}/TPPO-bound warm structures. In the Ca^{2+}-free cold conformation, R1072 is displaced from the S1–$S4_{Upper}$ pocket and stabilized by an interaction with Q831 on S2—a key residue involved in Ca_{TMD} binding—thereby precluding TPPO binding (Fig. 3e). Upon transition to the warm state, upward movement of the intracellular domain tilts the TRP helix, moving R1072 into position for TPPO coordination (Fig. 3e). Concurrently, Ca^{2+} binding at the Ca_{TMD} site recruits Q831 for Ca^{2+} coordination, releasing R1072 from its locked pose for direct interaction with the TPPO phosphoryl group (Fig. 3e). Together, these coupled rearrangements prime the S1–$S4_{Upper}$ pocket for effective ligand engagement.

Interestingly, a weak TPPO-shaped density was also detected in the minor Ca^{2+}-bound cold conformation present in the Ca^{2+}/TPPO–TRPM4–37°C dataset, identified through single-subunit classification (Extended Data Fig. 4). This density was weaker than in the warm conformation but stronger than in the corresponding Ca^{2+}-bound cold conformation resolved at 18°C (Fig. 3b, lower panel; Fig. 3d; Extended Data Fig. 6), indicating that TPPO occupancy increases with temperature even within the same overall protein conformation. Because the backbone architecture of the binding site remains nearly identical between the two cold structures, this enhancement likely arises from subtle, temperature-dependent sidechain rearrangements—below

246 the resolution of our maps (~2.6 Å local)—that fine-tune ligand packing and render the
247 interaction thermodynamically more favorable.

248 Together, these results reveal that TPPO selectively engages the warm conformation of
249 TRPM4 by exploiting temperature- and Ca^{2+}-dependent changes in local binding energetics. This
250 provides a direct structural basis for the observed three-way synergy, illustrating how intrinsic
251 modulators reshape the binding pocket to control ligand efficacy at the atomic level.

252 **Mechanistic basis for Ca^{2+}-dependent gating reversal of NC1**

253 Building on our observation that NC1 activates TRPM4 in the absence of Ca^{2+} but loses efficacy
254 once Ca^{2+} reaches activating levels (Fig. 2a–f), we sought to define the structural basis of this
255 gating reversal. To this end, we determined cryo-EM structures of TRPM4 in complex with NC1
256 at 37 °C under Ca^{2+}-free and Ca^{2+}-bound conditions, resolved to 2.6 and 2.8 Å, respectively
257 (Extended Data Figs. 7; Supplementary Fig. 1; Supplementary Data Table 2).

258 In the Ca^{2+}-free dataset, a well-defined tripod-shaped density was observed in the S1–S4
259 domain (~2.6 Å local resolution), occupying the same pocket as the TPPO and deacetyl
260 bisacodyl binding sites[25], while no Ca^{2+} density appeared at the Ca_{TMD} site, as expected (Fig. 4a).
261 The shape and dimensions of this density unambiguously matched NC1, which, despite being
262 larger than TPPO, adopts a comparable three-ring scaffold with its indolinone carbonyl oxygen
263 positioned analogously to TPPO's phosphoryl oxygen (Figs. 3d, left panel; Fig. 4a).
264 Consequently, NC1 binds in a similar pose to TPPO, engaging an equivalent network of residues,
265 including a key polar contact between its indolinone carbonyl oxygen and R1072 on the TRP
266 helix (Fig. 4a). Consistent with this, alanine substitution of R1072 and other residues within the
267 binding site abolished or markedly reduced NC1-mediated activation (Fig. 4c; Extended Data
268 Fig. 3b), confirming that NC1, like TPPO, binds to the S1–$S4_{Upper}$ site.

269 Interestingly, in the Ca^{2+}-bound dataset, NC1 density at the same S1–$S4_{Upper}$ pocket was
270 markedly weaker (Fig. 4b). This diminished occupancy aligns with our electrophysiological
271 findings, where 1 uM Ca^{2+} strongly suppressed the linear, NC1-evoked currents characteristic of
272 Ca^{2+}-free conditions and restored the canonical Ca^{2+}-dependent gating pattern (Fig. 2a–f).
273 Together, these data indicate that NC1 binding is strongly disfavored in the presence of Ca^{2+}.
274 While we cannot exclude the possibility that NC1 and Ca^{2+} may co-bind and produce an

electrophysiological profile similar to Ca^{2+} alone, the pronounced weakening of NC1 density in the Ca^{2+}-bound structures suggests that a Ca^{2+}-dependent reduction, or near abolition, of NC1 binding is the most likely explanation. Accordingly, we interpret the weak residual density as arising from the oversaturating NC1 concentration used for cryo-EM rather than from stable co-binding. Importantly, the antagonism does not result from direct competition for a shared site but instead from allosteric interference between the NC1 pocket and the Ca_{TMD} site (Fig. 4b).

To understand the basis of this interference, we compared the Ca^{2+}-free NC1–TRPM4 and Ca^{2+}–TRPM4 complexes. Two local structural changes accompany Ca^{2+} coordination at the Ca_{TMD}. First, Ca^{2+} binding repositions the TRP helix, shifting R1072 away from the indolinone carbonyl oxygen that is central to NC1 recognition (Fig. 4d). Second, Ca^{2+} binding brings the positively charged R905 into close proximity with NC1's hydrophobic seven-membered cycloheptyl ring, creating an electrostatically unfavorable juxtaposition that further destabilizes ligand binding (Fig. 4d). Together, these antagonistic rearrangements explain why NC1 affinity drops at increased Ca^{2+} concentration.

In summary, NC1 represents the first example of a TRPM4 activator that is temperature-independent yet negatively regulated by intrinsic Ca^{2+}. Structural and functional analyses together uncover a Ca^{2+}-dependent gating reversal, whereby Ca^{2+} reshapes the allosteric network to displace a previously bound activator. This mechanism contrasts sharply with TPPO, whose efficacy requires Ca^{2+} synergy at physiological temperature, underscoring the opposing logic by which intrinsic modulators shape TRPM4 pharmacology.

NC1 overrides Ca^{2+}-dependent ICD–TMD allosteric regulation

The defining feature of NC1 is that it activates TRPM4 without requiring Ca^{2+} at either of the two regulatory sites (Fig. 2a,d): the agonist site Ca_{TMD} and the temperature-dependent allosteric site in the intracellular domain (Ca_{ICD}). In canonical gating, Ca^{2+} and temperature cooperatively couple the ICD and TMD to drive activation: Ca^{2+} binding at the temperature-sensitive Ca_{ICD} shifts the channel from the cold to the warm state, establishing the primed conformation in which Ca^{2+} binding at the Ca_{TMD} opens the pore at physiologically relevant membrane potentials[10]. To understand how NC1 circumvents this mechanism, we compared three structural states: Ca^{2+}-free cold, Ca^{2+}-bound warm, and NC1-bound. The transition from Ca^{2+}-free cold to Ca^{2+}-bound warm involves major ICD rearrangements coupled to a substantial shift in the TRP helix and TMD

305 (Fig. 4e). By contrast, in the NC1-bound structure the ICD remains in the cold-like, yet the TMD
306 closely resembles the warm state conformation even in the absence of Ca^{2+} at the Ca_{TMD} (Fig.
307 4f). These observations suggest that NC1 functionally substitutes for Ca^{2+} at the TMD while
308 operating independently of Ca^{2+}-dependent priming at the ICD.

309 Electrophysiology supported this model: NC1 elicited robust currents of comparable
310 amplitude at both room and physiological temperatures (Fig. 2b,e)—in contrast to Ca^{2+}-
311 dependent TRPM4 activation, which is strongly enhanced at 37 °C through Ca_{ICD}-mediated
312 ICD–TMD coupling[10,15]. Thus, NC1 activates the channel without engaging the Ca_{ICD}-driven
313 allosteric control. To directly test this mechanism, we examined the E396A mutant, which
314 abolishes Ca_{ICD} binding and locks TRPM4 in the cold-like conformation regardless of
315 temperature[10]. Remarkably, NC1 still produced strong, temperature-independent activation in
316 this mutant, confirming that NC1 does not require the ICD–TMD regulation (Extended Data Fig.
317 3c). This unprecedented mode of action reveals an alternative allosteric pathway within TRPM4
318 and highlights NC1 as a promising scaffold for therapeutic development, particularly under
319 conditions where intracellular Ca^{2+} fluctuates.

320 **NBA and CBA inhibit TRPM4 through the S1–S4$_{Lower}$ site**

321 Pharmacological inhibition of TRPM4 is of broad clinical importance, as channel overactivation
322 contributes to arrhythmogenic cardiac disorders, ischemic injury, and cancer progression[18,21,38].
323 However, our previous work revealed that the endogenous antagonist ATP markedly loses
324 potency at physiological temperature because its binding location shifts between the cold and
325 warm conformations of the channel[10]. This temperature sensitivity limits ATP's ability to
326 suppress TRPM4 under normal cellular conditions[39].

327 To identify inhibitors that remain effective within the physiological conformational
328 landscape, we turned to NBA and its analog CBA[37]. In contrast to ATP and other temperature-
329 sensitive ligands, NBA and CBA inhibit TRPM4 in a temperature-independent manner,
330 maintaining high potency at 37 °C (Extended Data Fig. 2a). This makes them ideal probes for
331 uncovering how TRPM4 inhibition can be achieved under physiological conditions through a
332 temperature-insensitive mechanism.

333 At 37 °C in the presence of Ca^{2+}, cryo-EM analysis of TRPM4 in complex with NBA or CBA
334 uncovered a previously unknown ligand binding site within the S1–S4 domain in both datasets,
335 present in both cold and warm conformations (Extended Data Figs. 8; Supplementary Fig. 1).
336 This site lies below the Ca_{TMD} site and adjacent to the S1–$S4_{Upper}$ pocket that accommodates
337 TPPO and NC1, and is therefore termed S1–$S4_{Lower}$ site (Fig. 5a,b). The ligand densities were of
338 excellent quality (local resolution ~2.6 Å) and matched the chemical structures of NBA and
339 CBA, respectively, allowing unambiguous ligand placement (Supplementary Fig. 1; Extended
340 Data Fig. 9a,b; Supplementary Tables 2, 3). In both inhibitors, the chlorophenyl-carboxyl group
341 points upward within the S1–S4 domain, with its carbonyl stabilized by two positively charged
342 residues, R905 on S4 and R1072 on the TRP helix (Fig. 5a,b).

343 Surprisingly, this S1–$S4_{Lower}$ site differs from the NBA binding site previously reported based
344 on lower-resolution cryo-EM maps[40], which placed the inhibitor ~10 Å away on the opposite
345 face of the S4 helix (Extended Data Fig. 9c)—within the cleft between the S1–S4 domain and
346 the pore domain (Extended Data Fig. 9d), analogous to the vanilloid pocket in TRPV channels
347 and the NDNA site in TRPM5[41,42]. Careful inspection of both regions in our high-resolution
348 maps revealed no evidence supporting that earlier assignment. Instead, in our NBA- and CBA-
349 bound structures, the vanilloid pocket consistently displayed the same Y-shaped density seen in
350 apo, TPPO-, and NC1-bound structures, indicating a tightly bound endogenous lipid rather than
351 inhibitor occupancy (Extended Data Fig. 9e).

352 To validate the S1–$S4_{Lower}$ pocket functionally, we introduced mutations at key interacting
353 residues and examined their effects using patch-clamp recordings. Substitution of either R905 or
354 R1072 by alanine completely abolished inhibition (Fig. 5c,d). Moreover, the second aromatic
355 group, a chlorophenyl in CBA or the bulkier naphthyl in NBA, extends downward into a cavity
356 formed between the S4–S5 linker and the TRP helix (Fig. 5a,b). Mutation of Q1061, positioned
357 near this distal aromatic moiety, also markedly reduced inhibition (Fig. 5c,d).

358 Together, these results establish the S1–$S4_{Lower}$ pocket as the functional binding site for NBA
359 and CBA, defining a second pharmacologically active locus within the S1–S4 domain. This
360 domain thus emerges as a bifunctional pharmacological hub in TRPM4, accommodating
361 both activators (TPPO, NC1, Ca^{2+}) and inhibitors (NBA, CBA) through spatially segregated
362 upper and lower sites that converge on shared gating residues such as R1072 on the TRP helix

363 (Fig. 5e). Consistent with this model, mutation of N786—a residue located within the S1–$S4_{Upper}$
364 region—abolished NC1 activation while leaving NBA-mediated inhibition largely intact
365 (Extended Data Fig. 2c,d). This uncoupling provides functional evidence that the upper and
366 lower S1–S4 pockets are partially independent, despite their close spatial proximity, and can
367 differentially engage ligands to produce distinct pharmacological outcomes.

368 **NBA and CBA inhibit TRPM4 by locking a pre-open conformation**

369 To elucidate how NBA and CBA inhibit Ca^{2+}-dependent activation, we first examined the
370 conformational transitions that underlie canonical TRPM4 gating. In the Ca^{2+}-free cold state,
371 W864 on S3 and H908 on S4 form a stabilizing π–π stacking interaction[43-45]. Upon Ca^{2+} binding,
372 coordinated engagement of the Ca_{TMD} and Ca_{ICD} triggers rearrangements in the S1–S4 bundle
373 and TRP helix, repositioning W864 and H908 and thereby disrupting the contact between the
374 intracellular tips of the S3 and S4 helices (Fig. 5f, the gray structure)—a hallmark of Ca^{2+}-gated
375 TRPM channel activation[42,46]. This frees the S4–S5 linker, allowing the S5–S6 pore domain to
376 open[10].

377 In the Ca^{2+}/NBA- and Ca^{2+}/CBA-bound structures, this transition is blocked. The distal
378 aromatic moiety of NBA or CBA occupies the position normally adopted by H908 in the
379 activated state, thereby forcing H908 to remain in its apo-like conformation. As a result, H908,
380 W864, and the ligand form a π–π–π triple stacking interaction that restrains the S4–S5 linker and
381 prevents pore opening (Fig. 5f, the purple structure). The overall architecture of the inhibited
382 state closely matches the Ca^{2+}-bound warm closed conformation (backbone RMSD 0.7 Å),
383 indicating that NBA and CBA trap TRPM4 in a Ca^{2+}-primed but non-conductive pre-open state.

384 To test this model, we used decavanadate (DVT), a positive modulator that we previously
385 showed binds at the ICD–TMD interface and facilitates the transition of TRPM4 from a Ca^{2+}-
386 bound pre-open state to the open state by pulling the pore-lining S6 helix to open the ion-
387 conducting pore[10,47]. Importantly, DVT binding—and the subsequent transition from the pre-
388 open to the open state—is accompanied by an upward tilting of the intracellular domain toward
389 the transmembrane domain[10]. We therefore reasoned that if NBA/CBA stabilize a Ca^{2+}-bound
390 pre-open state, they should prevent the conformational changes required for DVT binding and
391 activation, or even preclude DVT binding altogether. To test this prediction, we determined the
392 structure of TRPM4 in the presence of Ca^{2+}, DVT, and CBA at 37 °C (Supplementary Fig. 1;

393 Extended Data Fig.10a; Supplementary Table 3). The resulting map contained densities only for
394 Ca^{2+} and CBA, with no evidence of DVT binding, and the protein conformation was identical to
395 the Ca^{2+}/CBA-bound closed state (Extended Data Fig. 10b). These data provide direct structural
396 evidence that DVT cannot override NBA/CBA inhibition, supporting our proposed inhibitory
397 mechanism.

398 Interestingly, this mechanism converges with that of ATP, which also prevents opening by
399 stabilizing the pre-open state, albeit through a distinct intracellular binding site[10]. Unlike ATP,
400 however, NBA and CBA act from the extracellular side and maintain high potency at
401 physiological temperature, offering both accessibility and stability within the native
402 conformational landscape. Thus, NBA and CBA represent promising scaffolds for the design of
403 TRPM4 inhibitors with therapeutic potential.

404 **Discussion**

405 This study reveals that TRPM4 pharmacology is not static but dynamically shaped by the
406 physiological environment, with temperature and intracellular Ca^{2+} acting as active determinants
407 of ligand binding, efficacy and mechanism. By integrating single-particle cryo-EM and
408 electrophysiology, we reveal that these intrinsic factors cooperatively remodel the
409 conformational landscape of TRPM4, exposing latent binding sites and revealing context-
410 dependent pharmacological behaviors that are obscured under non-physiological conditions.

411 Physiological context unmasks the true pharmacological profiles of ligands. The small
412 molecule TPPO, long regarded as a TRPM5-specific inhibitor, emerges here as a potent activator
413 of TRPM4, but only when both temperature and intracellular Ca^{2+} reach physiological levels
414 (Fig. 6a). Conversely, NC1, previously characterized as a Ca^{2+}-independent agonist, undergoes a
415 functional reversal: at basal Ca^{2+} it activates TRPM4, whereas at elevated Ca^{2+} it becomes
416 functionally antagonized, manifesting as little to no additional effect beyond Ca^{2+} alone,
417 revealing an unexpected inhibitory facet of Ca^{2+} regulation (Fig. 6b). Mechanistically, these
418 contrasting behaviors arise because temperature and Ca^{2+} cooperatively determine the
419 equilibrium between cold and warm conformations of TRPM4, thereby governing access to key
420 residues within the S1–S4 regulatory domain. Thus, ligand efficacy in TRPM4 is not an intrinsic
421 property of the compound alone, but an emergent consequence of its interplay with the
422 conformational and thermodynamic landscape of the channel.

423 Moreover, our structural analyses establish the S1–S4 domain as a versatile pharmacological
424 hub that integrates both environmental and chemical inputs. Within this domain, around the
425 Ca_{TMD} site, two spatially distinct but functionally coupled sites control opposite gating outcomes:
426 the $S1–S4_{Upper}$ pocket, occupied by activators TPPO, NC1, and deacetyl bisacodyl[25]; and the S1–
427 $S4_{Lower}$ pocket, targeted by inhibitors NBA and CBA (Fig. 5e). Both pockets converge on the
428 TRP helix through the conserved residue like R1072 on the TRP helix, which serves as a central
429 allosteric node linking environmental cues to gating transitions. Ligand engagement at the upper
430 pocket promotes activation by coupling between the S1–S4 domain and the pore domain,
431 whereas ligand binding to the lower pocket disrupts this coupling, stabilizing a non-conductive
432 state. This dual-site organization provides a unified explanation for how temperature, Ca^{2+} and
433 chemically diverse ligands—activators and inhibitors alike—modulate TRPM4 through a shared
434 structural framework. Of note, our TPPO- and NC1-bound cryo-EM structures capture TRPM4
435 in a closed pore conformation, consistent with our previous observations that the pore remains
436 closed in the presence of the endogenous activator Ca^{2+} alone. These observations suggest that
437 agonist engagement with the S1–S4 domain, while necessary for activation, is not sufficient to
438 stabilize an open pore under cryo-EM conditions, likely due to the absence of membrane
439 potential. In contrast, open-pore conformations have been observed in the presence of additional
440 modulators, such as DVT or PIP_2, which render the channel voltage independent[10,48].

441 This regulatory logic uncovered here may represent a general feature of TPRM channels. In
442 TRPM3 and TRPM5, both agonists and antagonists occupy the upper pocket[49-51]; and in TRPM8,
443 ligands engage both[52-54]. The S1–S4 domain thus exemplifies an evolutionary design in which
444 temperature and chemical cues dynamically reconfigure a common structural scaffold to yield
445 distinct, context-dependent functional outcomes.

446 Notably, we found that temperature-dependent ligand recognition in TRPM4 is not limited to
447 regions that undergo large-scale rearrangements. Even sites within structurally stable domains—
448 such as the S1–S4 transmembrane bundle, which exhibits only subtle temperature-driven
449 movements—can undergo marked shifts in ligand accessibility and efficacy. This principle likely
450 extends to many drug targets, highlighting that seemingly rigid structural regions may harbor
451 cryptic, environment-sensitive pharmacology.

More broadly, these findings support an environment-aware framework of pharmacology, in which physiological variables such as temperature and intracellular Ca^{2+} act as active modulators of ligand binding, potency, and efficacy rather than as passive background conditions. At present, however, the extent to which this principle applies across proteins more generally remains underexplored. Modulation of ligand binding by temperature—and potentially by Ca^{2+} or other physiological cofactors—has historically received limited attention, and relatively few explicit examples are available.

Nevertheless, precedent exists. Crystallographic studies of PBP1B have shown that ligands adopt distinct binding poses when structures are determined at cryogenic versus room temperatures[55], and analogous temperature-dependent side-chain rearrangements upon metal binding have been observed in hen egg white lysozyme[56]. Similarly, a recent study of ionotropic glutamate receptors has shown that glutamate-dependent pore opening is strongly promoted at physiological temperatures, allowing activated states to be captured by cryo-EM that were not observed in samples prepared under non-physiological temperature conditions[9]. Together with these examples, our results suggest that pharmacological specificity may emerge from the interplay between ligand chemistry and the dynamic, context-dependent structural state of the target protein. We propose that extending similar approaches to other ion channels and proteins will be an important direction for future work, with potential implications for bridging the gap between in vitro pharmacological screening and in vivo drug performance.

For ubiquitously expressed proteins such as TRPM4, these principles carry important therapeutic implications. By exploiting local physiological changes—such as elevated intracellular Ca^{2+} during stress or altered thermal states in disease—future drugs could be tailored to act selectively in pathological contexts while sparing normal function. Such environment-sensitive design strategies may reduce side effects and offer a new route toward precision pharmacology.

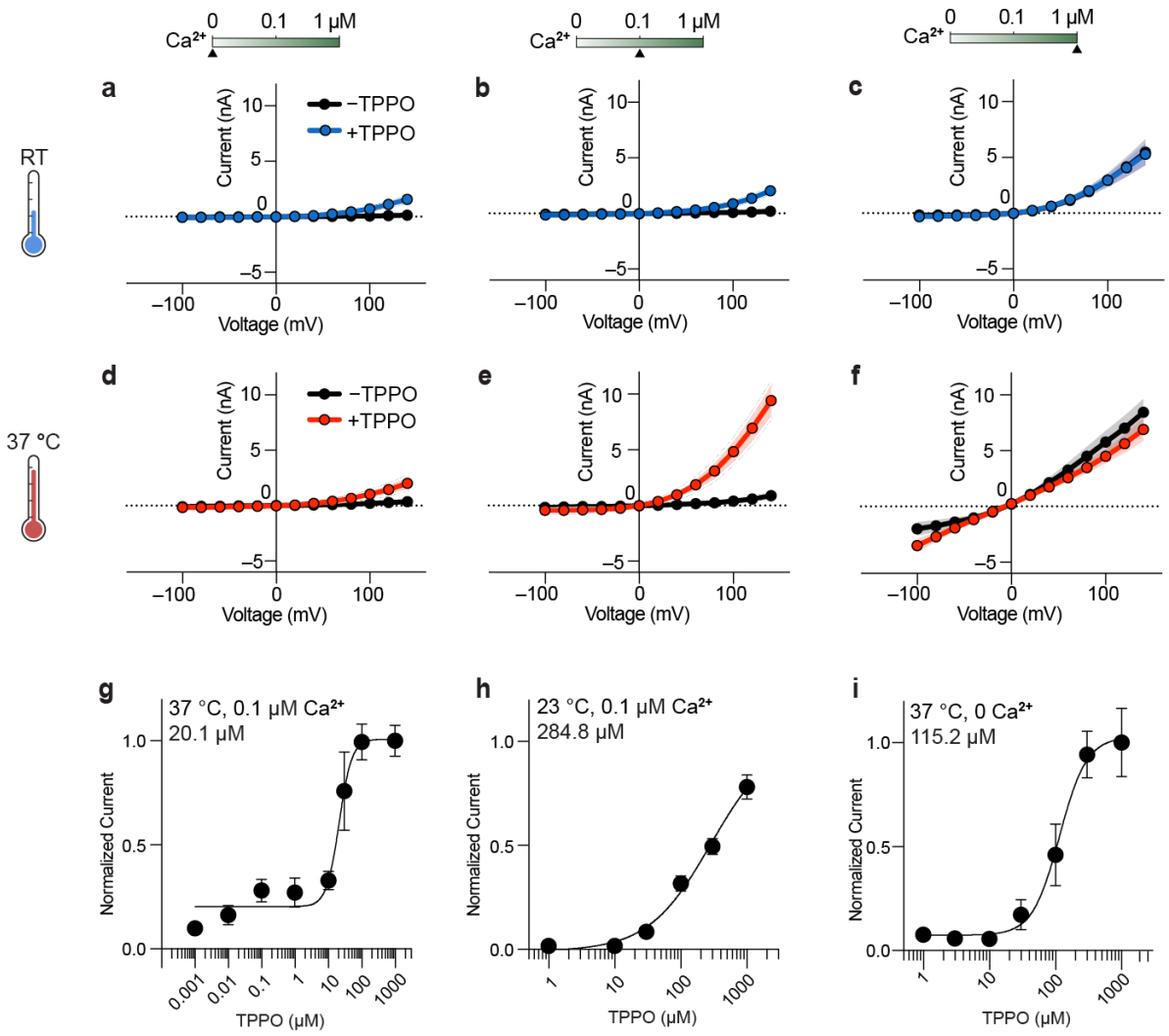

Figure 1. Three-way synergy between TPPO, temperature and Ca^{2+}.

a–f, Whole-cell currents measured in tsA cells overexpressing wild-type TRPM4 at 22 °C (upper panels) and 37 °C (lower panels), with free intracellular Ca^{2+} concentrations of 0 μM (**a, d**), 0.1 μM (**b, e**) and 1 μM (**c, f**), in the absence or presence of 50 μM extracellular TPPO. A voltage protocol stepping from −100 mV to +140 mV in 20-mV increments was applied, with each voltage step lasting 100 ms. The currents from all measured cells were then averaged and plotted versus voltage to generate the mean I–V curve, with the line representing the mean and the shaded indicating the s.e.m. The numbers of independently measured cells are as follows: (**a**) n=9 (−TPPO) / 9 (+TPPO), (**b**) n=7 (−TPPO) / 8 (+TPPO), (**c**) n=9 (−TPPO) / 9 (+TPPO), (**d**) n=7 (−TPPO) / 10 (+TPPO), (**e**) n=8 (−TPPO) / 8 (+TPPO), and (**f**) n=6 (−TPPO) / 6 (+TPPO).

489 **g–i**, TPPO dose-response measurements for wild-type TRPM4 with 0.1 μM free intracellular
490 Ca^{2+} at 37 °C (**g**), 0.1 μM Ca^{2+} at 23 °C (**h**), and 0 μM Ca^{2+} at 37 °C (**i**). A voltage protocol was
491 applied every 10 s to monitor current changes: –100 mV for 200 ms, followed by +100 mV for
492 200 ms. Once the current stabilized at each TPPO concentration, the current amplitudes at +100
493 mV from all measured cells were averaged, and the mean amplitudes were plotted and fitted to
494 obtain the EC_{50}. Current amplitudes were normalized either to the mean at 1000 μM TPPO (**g, i**)
495 or to the fitted I_max from the Hill equation (**h**). Data are presented as mean ± s.e.m. The
496 numbers of independently measured cell are as follows: (**g**) n=7 for all concentrations, (**h**) n=5 at
497 1 μM and n=7 for all other concentrations, and (**i**) n=7 for all concentrations.

498

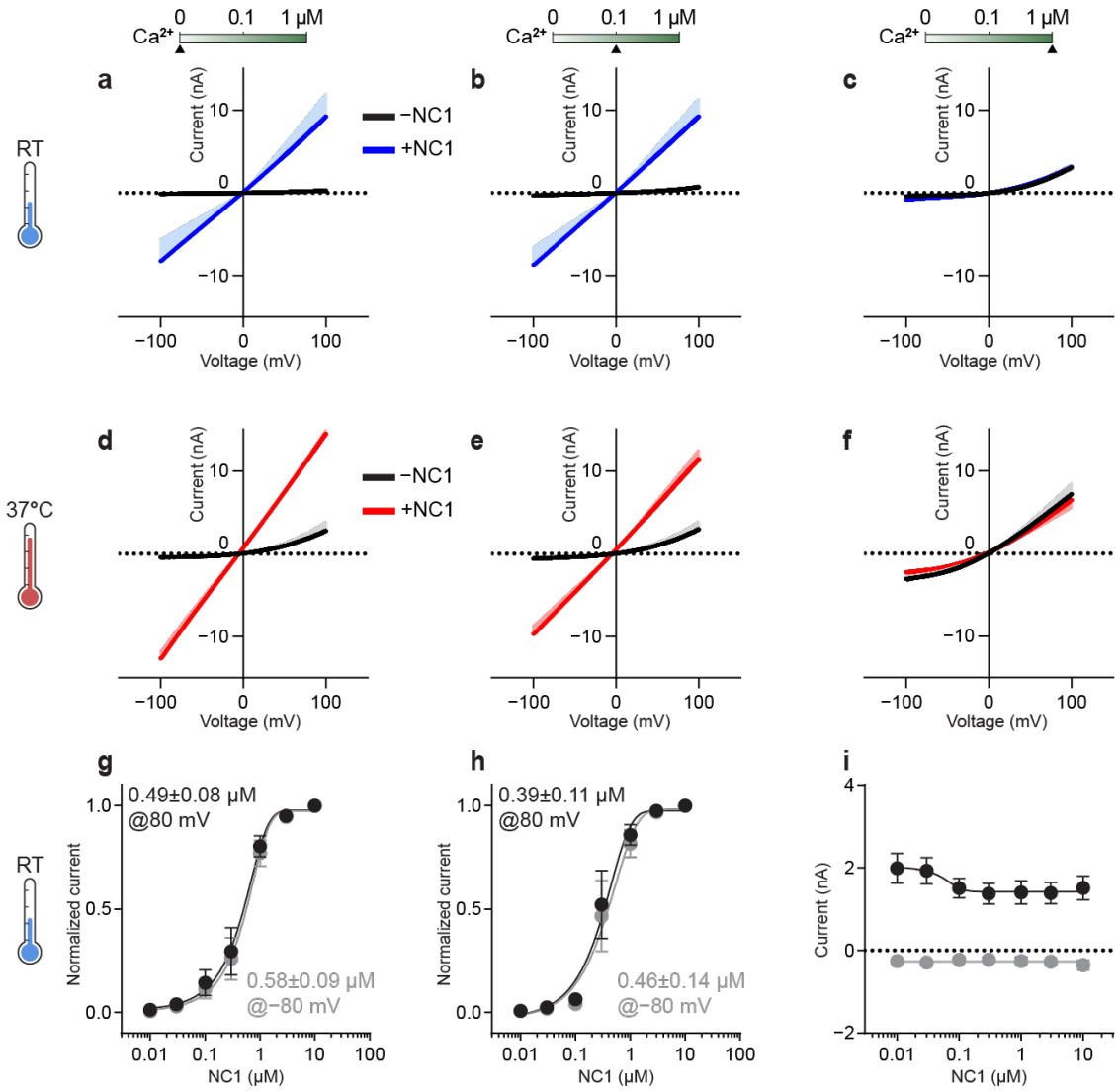

Figure 2. Ca^{2+}-dependent gating reversal of NC1.

a–f, Whole-cell currents measured in tsA cells overexpressing wild-type TRPM4 at 22 °C (upper panels) and 37 °C (lower panels), with free intracellular Ca^{2+} concentrations of 0 μM (**a, d**), 0.1 μM (**b, e**) and 1 μM (**c, f**). A voltage protocol was applied every 5 s to monitor current changes until reaching steady state: −100 mV for 50 ms, ramped to +100 mV over 200 ms and held at +100 mV for 50 ms. The currents without and with 1 μM extracellular NC1 in each condition were measured in a single cell. The currents from all measured cells were then averaged and plotted versus voltage to generate the mean I–V curve, with the line representing the mean and the shaded indicating the s.e.m. For clarity, the s.e.m. envelope was plotted in one direction. The numbers of independently measured cells are as follows: n=5 (**a**), n=7 (**b**), n=5 (**c**), n=5 (**d**), n=4

510 (**e**), and n=4 (**f**). **g–i**, NC1 dose-response measurements for wild-type TRPM4 at
511 22 °C with 0 μM free intracellular Ca^{2+} (**g**), 0.1 μM Ca^{2+} (**h**), and 1 μM Ca^{2+} (**i**). A voltage
512 protocol was applied every 5 s to monitor current changes: 0 mV for 50 ms, switch to +80 mV
513 for 50 ms, followed by −80 mV for 50 ms, and return to 0 mV for 50 ms. Once the current
514 stabilized at each NC1 concentration, the current amplitudes at +80 mV and −80 mV were
515 normalized to those at 10 μM NC1. Normalized currents from all measured cells were averaged
516 and plotted as mean ± s.e.m. EC_{50} values obtained from individual cells were averaged to yield
517 the final EC_{50} reported as mean ± s.e.m. (**g**,**h**). Data are presented as mean ± s.e.m. The numbers
518 of independently measured cells are as follows: n=5 (**g**), n=5 (**h**), and n=4 (**i**).

519

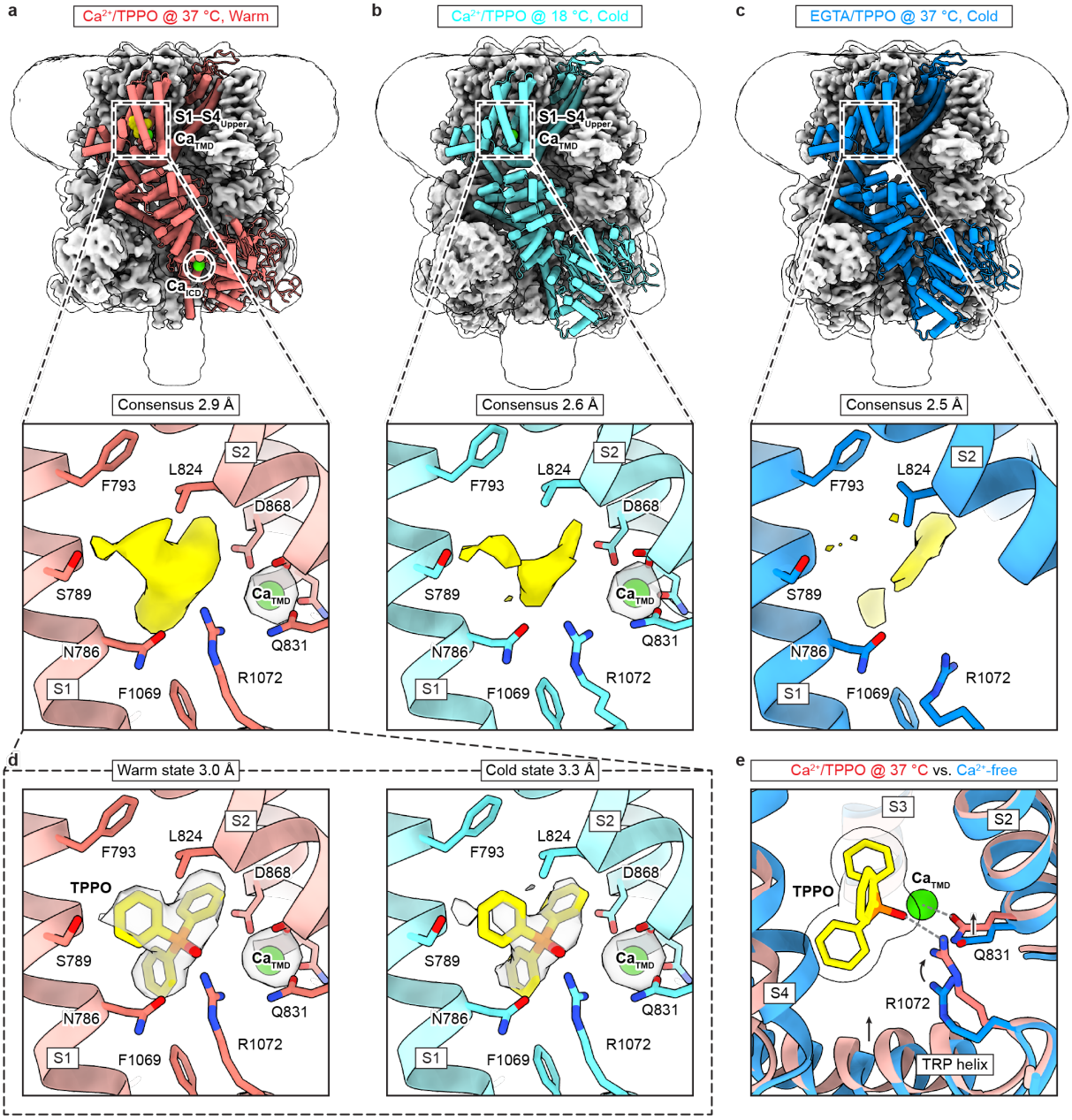

Figure 3. Structural basis of the three-way synergy between TPPO, temperature and Ca^{2+}.

a–c, Structures of TRPM4 in complex with Ca^{2+}/TPPO at 37 °C (**a**, PDB-ID 9Z1W), Ca^{2+}/TPPO at 18 °C (**b**, PDB-ID 9Z1Z), and EGTA/TPPO at 37 °C (**c**, PDB-ID 9Z20). One subunit is shown in cartoon representation, while the remaining three subunits are displayed as the cryo-EM map, viewed parallel to the membrane. The transparent envelope outlines the detergent micelle and the disordered region of the C-terminal coiled-coil. TPPO is highlighted in yellow and Ca^{2+} in green.

The resolution of the consensus map is indicated below. Bottom panels show the details of the S1–S4 binding site in the consensus maps. The protein backbone is shown in cartoon representation, with key interacting residues in stick representation. Densities at the TPPO binding site (yellow) and at the Ca_{TMD} site (transparent in **a**,**b**) are contoured at 4.5 σ. **d**, Details of the S1–S4 binding site in the warm (left, PDB-ID 9Z1X) and cold (right, PDB-ID 9Z1Y) states, obtained from classification of the Ca^{2+}/TPPO dataset collected at 37 °C. The resolution of each cryo-EM map is indicated. Densities at the TPPO binding site and the Ca_{TMD} site are shown as transparent surface representations contoured at 9 σ. The fitted TPPO molecule is shown in stick representation, and Ca_{TMD} as a green sphere. **e**, Structural comparison of TRPM4 with Ca^{2+}/TPPO at 37 °C (salmon, PDB-ID 9Z1X) and the Ca^{2+}-free apo state (blue, PDB-ID 9B93), superimposed using the S1–S4 (residues 760–910). TPPO is shown in stick representation with a transparent envelope, and Ca_{TMD} as a green sphere. Black arrows indicate the approximate direction of movement of key residues and the TRP helix. The dashed lines mark key interactions.

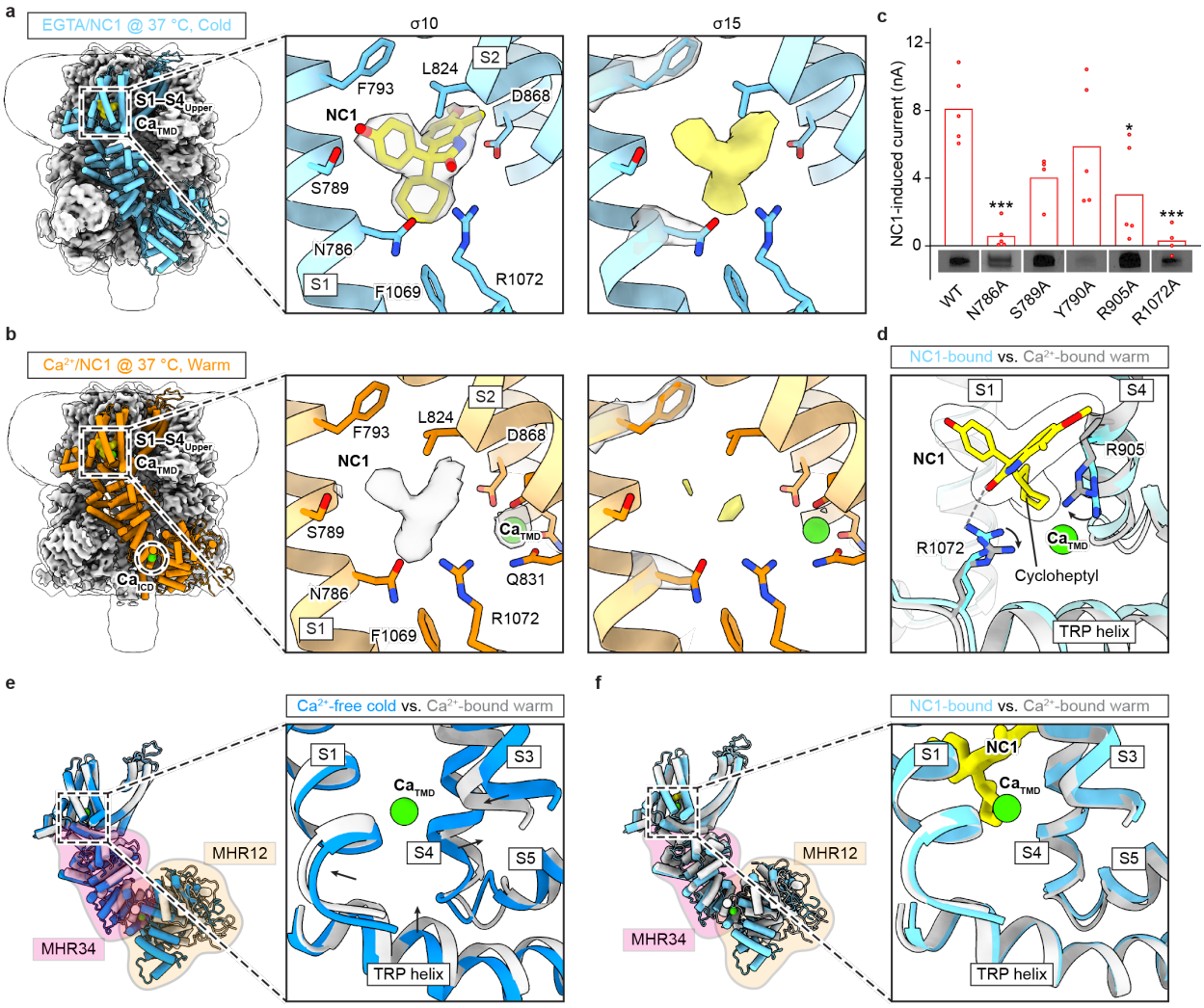

Figure 4. Mechanistic basis for Ca^{2+}-dependent gating reversal of NC1.

a,**b** The left panels show the structures of TRPM4 in complex with EGTA/NC1 at 37 °C (**a**, PDB-ID 9Z22) and Ca^{2+}/NC1 at 37 °C (**b**, PDB-ID 9Z21). One subunit is shown in cartoon representation, while the remaining three subunits are displayed as the cryo-EM map, viewed parallel to the membrane. The transparent envelope outlines the detergent micelle and the disordered region of the C-terminal coiled-coil. The middle panels show the details of the S1–S4 binding site, with the protein backbone in cartoon representation and key interacting residues in stick representation. Densities at the NC1 binding site, and at the Ca_{TMD} site (only in **b**) are shown as transparent surface representations contoured at 10 σ. The fitted NC1 molecule in (only in **a**) is shown in stick representation, and Ca_{TMD} as a green sphere (only in **b**). The right panels

present the same regions as the middle panels but additionally display densities for well-defined side chains within the binding site, contoured at 15 σ. **c**, NC1-induced whole-cell current amplitudes at +100 mV in cells overexpressing wild-type TRPM4 and binding-site mutants, calculated by subtracting the steady-state current recorded before NC1 application from that recorded after application. Each point represents an independently measured cell (n = 5 (WT), 5 (N786A), 4 (S789A), 5 (Y790A), 5 (R905A), 4 (R1072A)), with bars indicating the mean. Statistical analysis was performed using one-way ANOVA with Bonferroni's post hoc test, comparing each mutant with wild type (*$p<0.05$, ***$p<0.001$). Averaged raw data are shown in Extended Data Fig. 3b. Cell surface expression of wild-type TRPM4 and mutants is shown, confirming proper trafficking to the plasma membrane; uncropped gels are provided in Supplementary Fig. 2. **d**, Structural comparison of TRPM4 NC1-bound state (cyan, PDB-ID 9Z22) and the Ca^{2+}-bound warm state (blue, PDB-ID 9B8W) of TRPM4, superimposed using the S1–S4 (residues 760–910). NC1 is shown in stick representation with a transparent envelope, and Ca_{TMD} as a green sphere. Black arrows indicate the approximate direction of movement of key residues. The dashed line marks a key interaction. **e**, Structural comparison of a single subunit of the Ca^{2+}-free cold state (blue, PDB-ID 9B93) and the Ca^{2+}-bound warm state (grey, PDB-ID 9B8W) of TRPM4, superimposed using the S1–S4 (residues 760–910). MHR3/4 is outlined with a pink envelope and MHR1/2 with an orange envelope. The right panel shows details of the S1–S4 binding site and its surroundings. Ca_{TMD} is shown in a green sphere, and the black arrows indicate the movement of structural elements forming the binding site upon Ca^{2+} binding. **f**, Structural comparison of the NC1-bound state (cyan, PDB-ID 9Z22) and the Ca^{2+}-bound warm state (grey, PDB-ID 9B8W) of TRPM4. The structures are superimposed and displayed similarly to panel (**e**). NC1 is shown in stick representation, and Ca_{TMD} as a green sphere.

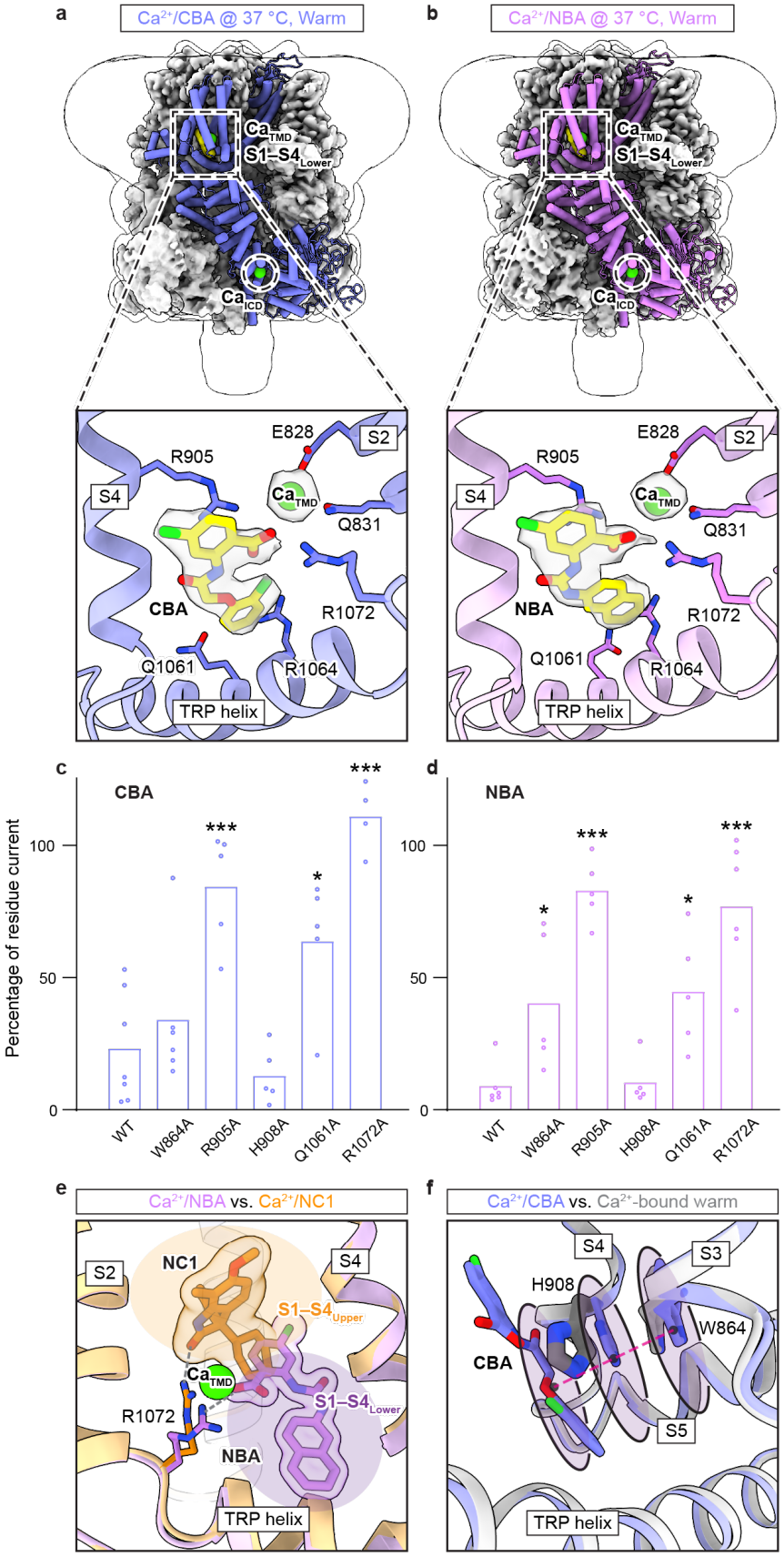
a
Ca2+/CBA @ 37 °C, Warm
b
Ca2+/NBA @ 37 °C, Warm
Ca TMD
S1–S4 Lower
Ca ICD
E828
S2
R905
S4
Ca TMD
Q831
CBA
R1072
Q1061
R1064
TRP helix
NBA
c
d
Percentage of residue current
100
50
0
WT
W864A
R905A
H908A
Q1061A
R1072A
e
Ca2+/NBA vs. Ca2+/NC1
NC1
S1–S4 Upper
S1–S4 Lower
f
Ca2+/CBA vs. Ca2+-bound warm
S3
H908
W864
S5

580

Figure 5. NBA and CBA inhibit TRPM4 through the S1–S4$_{Lower}$ site.

a,**b** Structure of TRPM4 in complex with Ca^{2+}/CBA at 37 °C (**a**, PDB-ID 9Z23) and Ca^{2+}/NBA at 37 °C (**b**, PDB-ID 9Z25). One subunit is shown in cartoon representation, while the remaining three subunits are displayed as the cryo-EM map, viewed parallel to the membrane. The transparent envelope outlines the detergent micelle and the disordered region of the C-terminal coiled-coil. CBA and NBA are highlighted in yellow and Ca^{2+} in green. Bottom panels show the details of the S1–S4 binding site, with the protein backbone in cartoon representation and key interacting residues in stick representation. Densities for CBA and Ca_{TMD} (**a**) and for NBA and Ca_{TMD} (**b**) are shown as transparent surface representations contoured at 17 σ and 20 σ, respectively. The fitted CBA and NBA molecules are shown in stick representation, and Ca_{TMD} as a green sphere. **c,d**, CBA- and NBA-dependent inhibition at +100 mV in cells overexpressing wild-type TRPM4 and binding-site mutants. The percentage of remaining currents after the application of NBA or CBA at 22 °C was calculated by dividing the steady-state current recorded after NBA or CBA application by the steady-state current recorded before application. Each point represents an independently measured cell: NBA, n = 6 (WT), 5 (W864A), 5 (R905A), 5 (H908A), 5 (Q1061A), and 6 (R1072A); CBA, n = 7 (WT), 6 (W864A), 5 (R905A), 5 (H908A), 5 (Q1061A), and 4 (R1072A). Bars indicate the mean. Statistical analysis was performed using one-way ANOVA with Bonferroni's post hoc test, comparing each mutant with wild type. (*$p<0.05$, ***$p<0.001$). Averaged raw data are shown in Extended Data Fig. 2b. **e**, Structural comparison of the Ca^{2+}/NBA-bound state (purple, PDB-ID 9Z26) and the NC1-bound state (orange, PDB-ID 9Z21) of TRPM4, superimposed using S1–S4 (residues 760–910). NBA and NC1 are shown in stick representation with a transparent envelope, and Ca_{TMD} as a green sphere. The filled orange and blue ellipses mark the upper and lower pockets within the S1–S4 domain, respectively. Arg1072 interacts with both ligands, as indicated by the dashed lines. **f**, Structural comparison of the Ca^{2+}/CBA-bound state (blue, PDB-ID 9Z23) and the Ca^{2+}-bound warm state (grey, PDB-ID 9B8W) of TRPM4, superimposed using S1–S4 (residues 760–910). CBA and the side chains of H908 and W864 are shown as stick representation, forming a triple stacking interaction indicated by the transparent discs and the red dashed line.

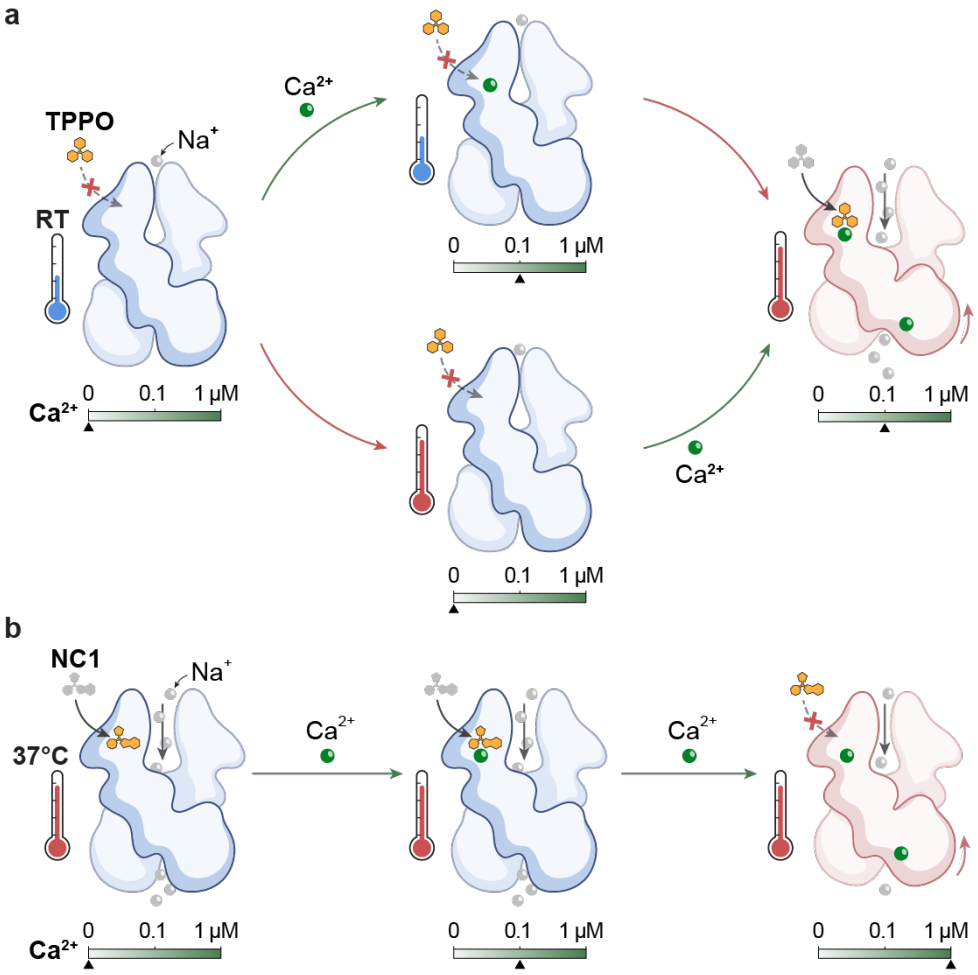

Figure 6. Distinct temperature- and Ca^{2+}-dependent activation mechanisms of TPPO and NC1 on TRPM4.

a, Schematic representation of the polymodal activation of TRPM4 by TPPO, Ca^{2+}, and temperature. Neither resting Ca^{2+} levels nor physiological temperature alone is sufficient to enable TPPO-mediated activation. Only when both resting Ca^{2+} and physiological temperature are present can TPPO exert its activating effect. **b**, Schematic representation of NC1 activity, which functions independently of Ca^{2+} at resting levels but loses efficacy once intracellular Ca^{2+} rises to stimulatory concentrations.

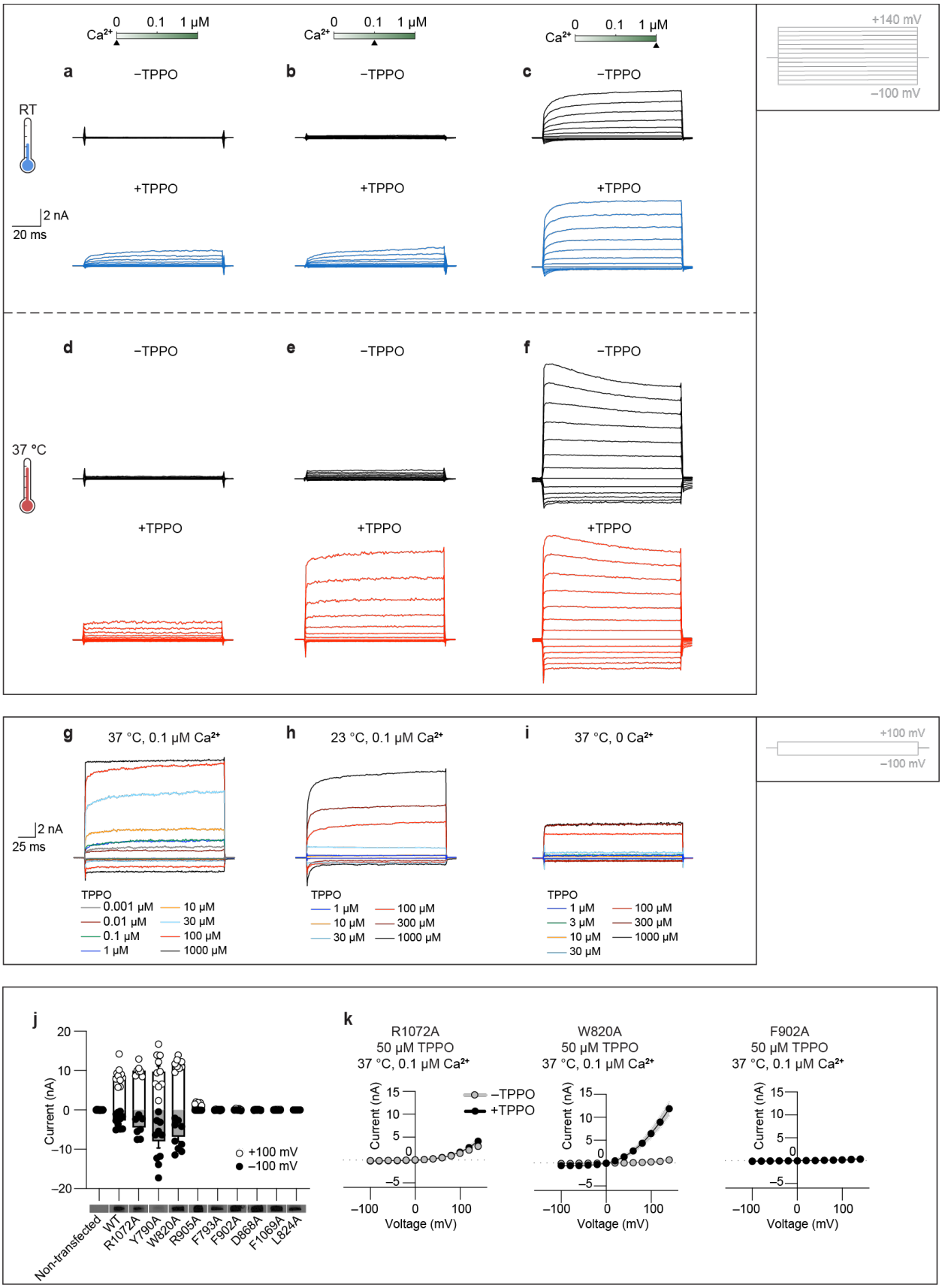
Ca2+ 0 0.1 1 μM
a
b
c
−TPPO
+TPPO
RT
2 nA
20 ms
+140 mV
−100 mV
d
e
f
37 °C
g
37 °C, 0.1 μM Ca2+
h
23 °C, 0.1 μM Ca2+
i
37 °C, 0 Ca2+
+100 mV
−100 mV
25 ms
TPPO
0.001 μM
0.01 μM
0.1 μM
1 μM
10 μM
30 μM
100 μM
1000 μM
3 μM
300 μM
j
Current (nA)
+100 mV
−100 mV
Non-transfected
WT
R1072A
Y790A
W820A
R905A
F793A
F902A
D868A
F1069A
L824A
k
R1072A
50 μM TPPO
37 °C, 0.1 μM Ca2+
W820A
F902A
−TPPO
+TPPO
Voltage (mV)

621 **Extended Data Figure 1. Electrophysiological characterization of TPPO-dependent**
622 **activation of TRPM4.**

623 **a–f**, Representative whole-cell current traces recorded at room temperature (23 °C) and 37 °C
624 with free intracellular Ca^{2+} concentrations of 0 μM (**a**,**d**), 0.1 μM (**b**,**e**), and 1 μM (**c**,**f**), evoked
625 by a voltage-step protocol from –100 mV to +140 mV in 20-mV increments (100 ms per step).
626 The currents without and with 50 μM extracellular TPPO at each condition were measured from
627 a single cell. **g–i**, Representative whole-cell current traces from the TPPO dose response
628 recordings acquired using a two-step protocol (–100 mV followed by +100 mV for 200 ms each)
629 under 0.1 μM Ca^{2+} at 37 °C (**g**), 0.1 μM Ca^{2+} at 23 °C (**h**), and 0 μM Ca^{2+} at 37 °C (**i**). **j**, Whole-
630 cell currents of non-transfected tsA cells and tsA cells overexpressing wild-type TRPM4 and
631 TPPO binding-site mutants evoked by 1 μM free intracellular Ca^{2+} and measured at +100 and
632 −100 mV at room temperature. Each point represents an independently measured cell: non-
633 transfected tsA201 (n=8), WT (n=10), R1072A (n=10), Y790A (n=7), W820A (n=10), W828A
634 (n=9), S789A (n=12), R905A (n=7), F793A (n=12), F902A (n=6), D868A (n=5), E898A (n=3),
635 F1069A (n=4), and L824A (n=5). Bars indicate the mean. Cell surface expression of wild-type
636 TRPM4 and mutants is shown, confirming proper trafficking to the plasma membrane;
637 uncropped gels are provided in Supplementary Fig. 2. **k,** Whole-cell currents measured in tsA
638 cells overexpressing the R1072A, W820A and F902A mutants at 37 °, with 0.1 μM free
639 intracellular Ca^{2+} in the absence or presence of 50 μM extracellular TPPO. A voltage protocol
640 stepping from −100 mV to +140 mV in 20-mV increments was applied, with each voltage step
641 lasting 100 ms. The currents from all measured cells were then averaged and plotted versus
642 voltage to generate the mean I–V curve, with the line representing the mean and the shaded
643 indicating the s.e.m. The numbers of independently measured cells are as follows: R1072A: n=9
644 (−TPPO) / 10 (+TPPO); W820A: n=10 (−TPPO) / 12 (+TPPO); F902A: n=8 (−TPPO) / 8
645 (+TPPO)).

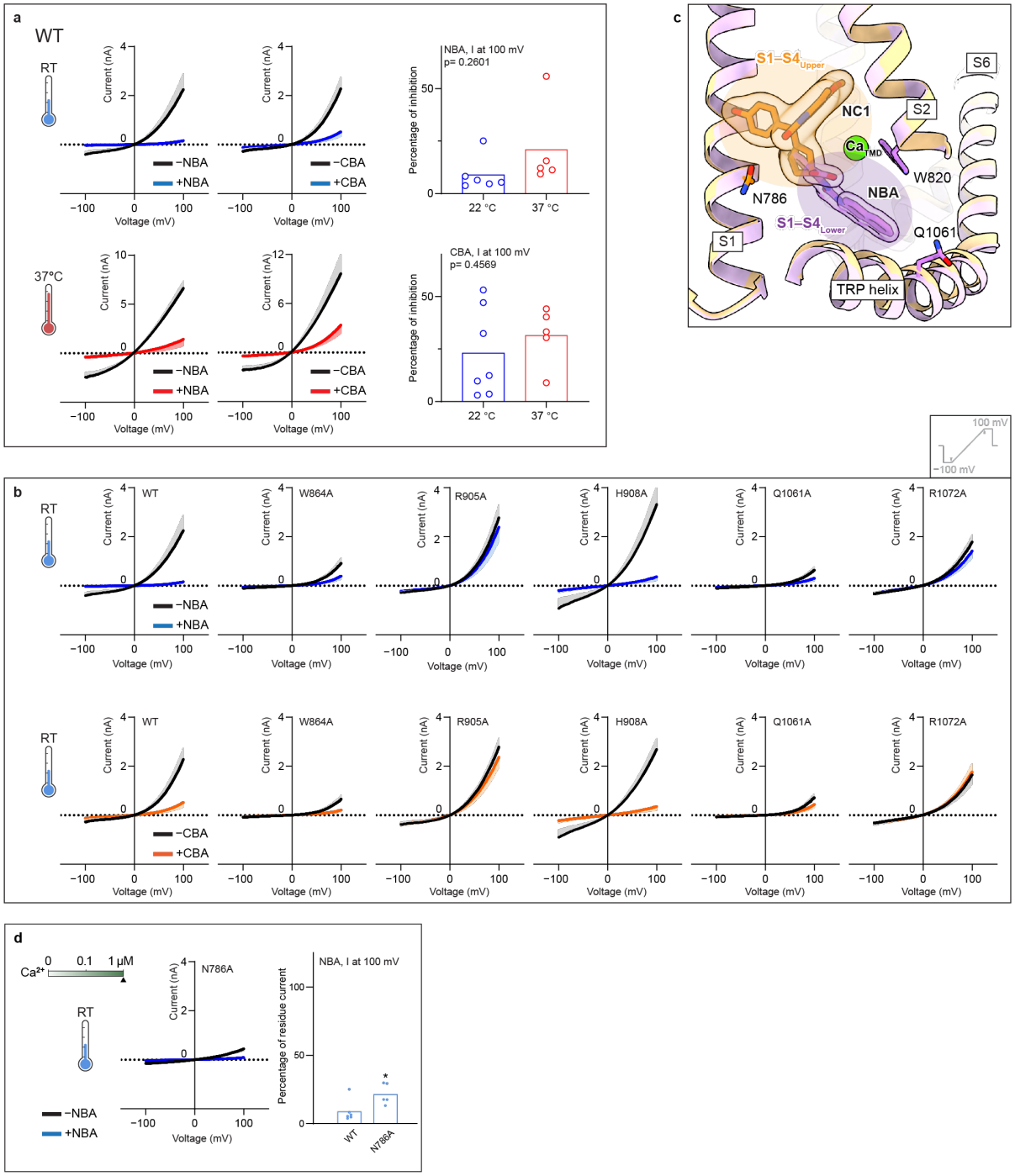

Extended Data Figure 2. Electrophysiological characterization of TRPM4 inhibition by NBA and CBA.

a, Left and middle panels show whole-cell currents measured in tsA cells overexpressing wild-type TRPM4 at 22 °C and 37 °C, with 1 μM free intracellular Ca^{2+}. A voltage protocol was

651 applied every 5 s to monitor current changes until reaching steady state: −100 mV for 50 ms,
652 ramped to +100 mV over 200 ms, and held at +100 mV for 50 ms. The currents without and with
653 10 μM extracellular NBA or CBA at each condition were measured from a single cell. The
654 currents from all measured cells were then averaged and plotted versus voltage to generate the
655 mean I–V curve, with the line representing the mean and the shaded indicating the s.e.m. For
656 clarity, the s.e.m. envelope was plotted in one direction. The numbers of independently measured
657 cells are as follows: n=6 (NBA, 22 °C), n=5 (NBA, 37 °C), n=7 (CBA, 22 °C), n=5 (CBA,
658 37 °C). Right panels show quantification of CBA- and NBA-dependent inhibition at +100 mV
659 for the recordings shown in the left and middle panels. The percentage of remaining currents
660 after the application of NBA or CBA was calculated by dividing the steady-state current recorded
661 after NBA or CBA application by the steady-state current recorded before application. Each
662 point represents an independently measured cell, and bars indicate the mean. A t-test was used to
663 compare inhibition at 22 °C versus 37 °C. **b**, Whole-cell currents measured in tsA cells
664 overexpressing wild-type TRPM4 or NBA/CBA binding-site mutants at 22 °C, with 1 μM free
665 intracellular Ca^{2+}, without and with 10 μM extracellular NBA or CBA. Measurements and
666 analysis were performed as in panel (**a**). The numbers of independently measured cells are as
667 follows. NBA: n=6 (WT), n=6 (W864A), n=5 (R905A), n=5 (H908A), n=6 (Q1061A), n=6
668 (R1072A); CBA: n=7 (WT), n=6 (W864A), n=5 (R905A), n=5 (H908A), n=5 (Q1061A), n=4
669 (R1072A). **c**, Structural comparison of the Ca^{2+}/NBA-bound state (purple, PDB-ID 9Z26) and
670 the NC1-bound state (orange, PDB-ID 9Z21) of TRPM4, superimposed using the S1–S4 domain
671 (residues 760–910). NBA and NC1 are shown in stick representation with a transparent
672 envelope, Ca_{TMD} as a green sphere and the protein backbone in cartoon representation and N786
673 side chain in stick representation. The filled orange and blue ellipses mark the upper and lower
674 pockets within the S1–S4 domain, respectively. **d**, Left panel shows whole-cell currents
675 measured in tsA cells overexpressing the N786A mutant at 22 °C, with 1 μM free intracellular
676 Ca^{2+}, without and with 10 μM extracellular NBA in the same cells (n=5). Right panel shows
677 quantification of NBA-dependent inhibition at +100 mV for wild-type TRPM4 and the N786A
678 mutant. Measurements and analysis were performed as in panel (**a**). Each point represents an
679 independently measured cell, and bars indicate the mean. The numbers of independently
680 measured cells are as follows: n = 6 (WT), 5 (N786A).

681

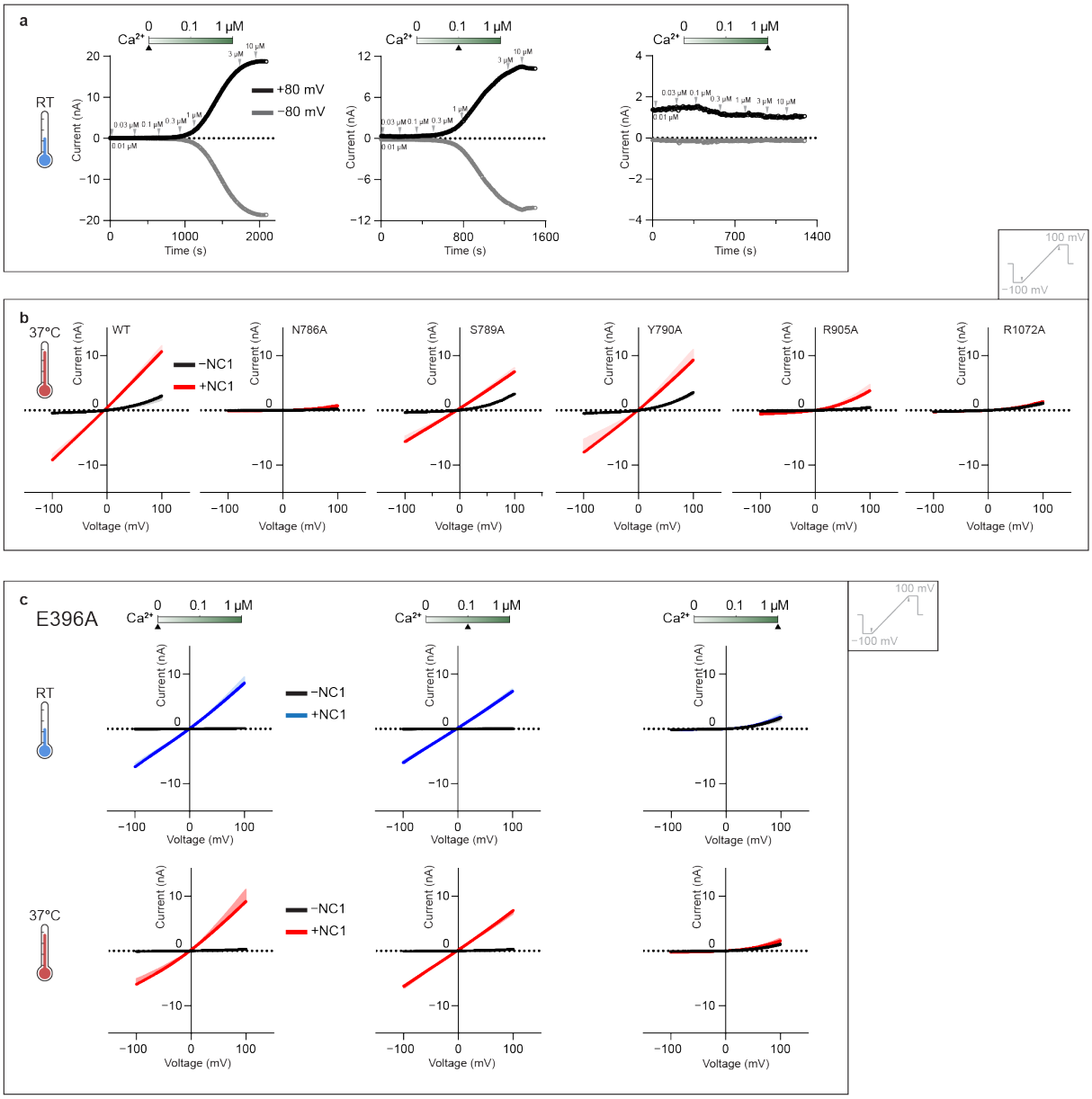

682

683 **Extended Data Figure 3. Electrophysiological characterization of NC1-dependent**
684 **activation of TRPM4.**

685 **a**, The representative current traces for the NC1 dose-response measurements for wild-type
686 TRPM4 at 22 °C with free intracellular Ca^{2+} of 0 μM, 0.1 μM, and 1 μM. A voltage protocol was
687 applied every 5 s to monitor current changes: 0 mV for 50 ms, switch to +80 mV for 50 ms,
688 followed by −80 mV for 50 ms, and return to 0 mV for 50 ms. **b**, Whole-cell currents measured
689 in tsA cells overexpressing wild-type TRPM4 or NC1 binding-site mutants at 37 °C, with 0.1 μM

free intracellular Ca^{2+}, without and with 1 μM extracellular NC1. A voltage protocol was applied every 5 s to monitor current changes until reaching steady state: −100 mV for 50 ms, ramped to +100 mV over 200 ms, and held at +100 mV for 50 ms. The currents without and with NC1 at each condition were measured from a single cell. The currents from all measured cells were then averaged and plotted versus voltage to generate the mean I–V curve, with the line representing the mean and the shaded indicating the s.e.m. For clarity, the s.e.m. envelope was plotted in one direction. The numbers of independently measured cells are as follows: n=5 (WT), n=5 (N786A), n=4 (S789A), n=5 (Y790A), n=5 (R905A), n=4 (R1072A). **c**, Whole-cell currents were measured in tsA cells overexpressing the E396A mutant of TRPM4 at 22 °C (upper panels) and 37 °C (lower panels), with intracellular free Ca^{2+} concentrations of 0 μM, 0.1 μM, and 1 μM. A voltage protocol was applied every 5 s to monitor current changes: −100 mV for 50 ms, ramped to +100 mV over 200 ms and held at +100 mV for 50 ms. The current without or with 1 μM extracellular NC1 in each condition was measured in a single cell. The currents from all measured cells were then averaged and plotted versus voltage to generate the mean I–V curve, with the line representing the mean and the shaded indicating the s.e.m. For clarity, the s.e.m. envelope was plotted in one direction. The numbers of independently measured cells are as follows: n=5 (0 μM Ca^{2+}, 22 °C), n=5 (0.1 μM Ca^{2+}, 22 °C), n=5 (1 μM Ca^{2+}, 22 °C), n=5 (0 μM Ca^{2+}, 37 °C), n=5 (0.1 μM Ca^{2+}, 37 °C) and n=5 (1 μM Ca^{2+}, 37 °C).

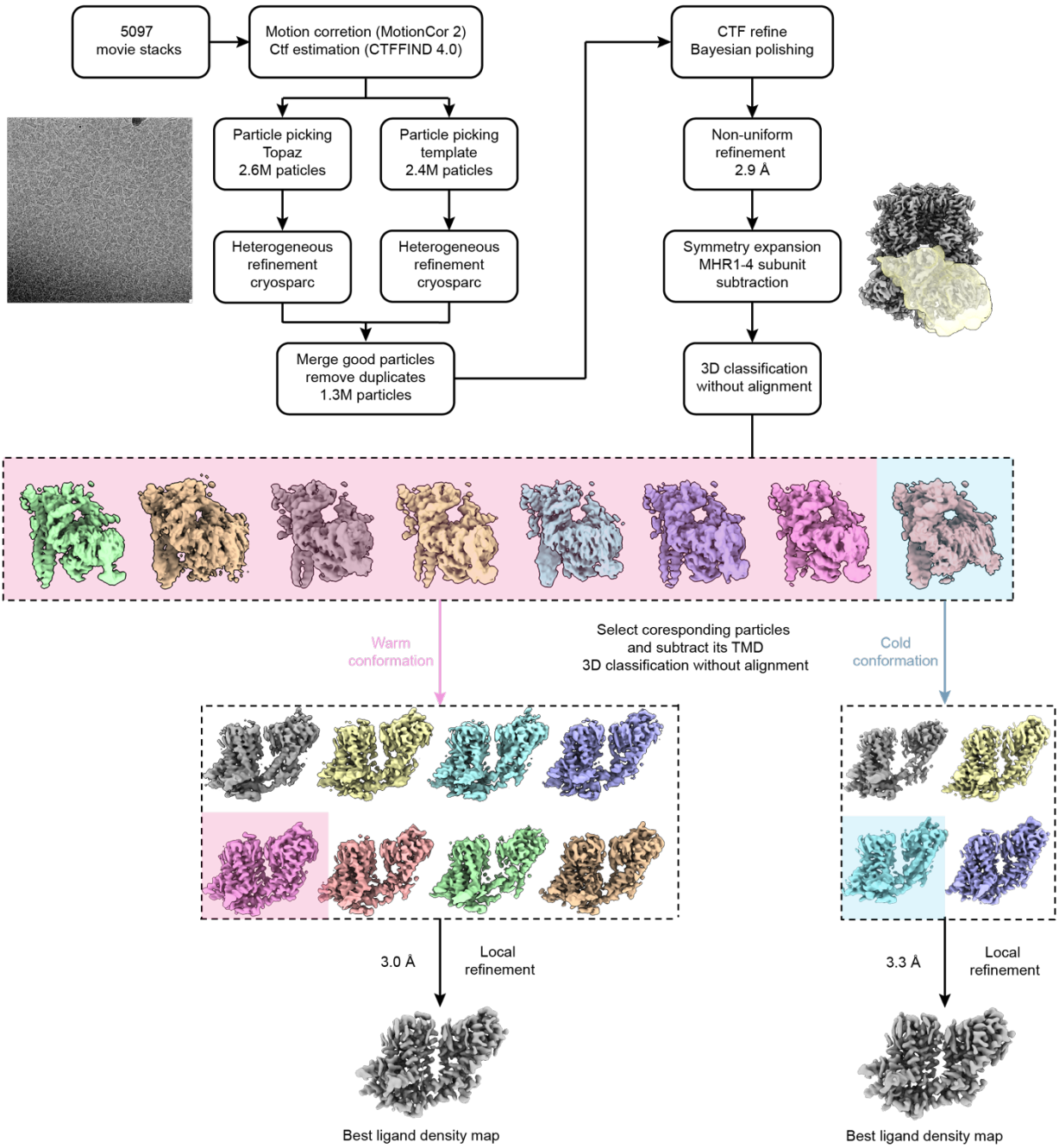

Extended Data Figure 4. Cryo-EM data processing workflow for the Ca^{2+}/TPPO–TRPM4–37 °C dataset. A representative micrograph is shown. The final consensus map and the TMD-focused map with the best-resolved ligand density are displayed with their respective resolutions.

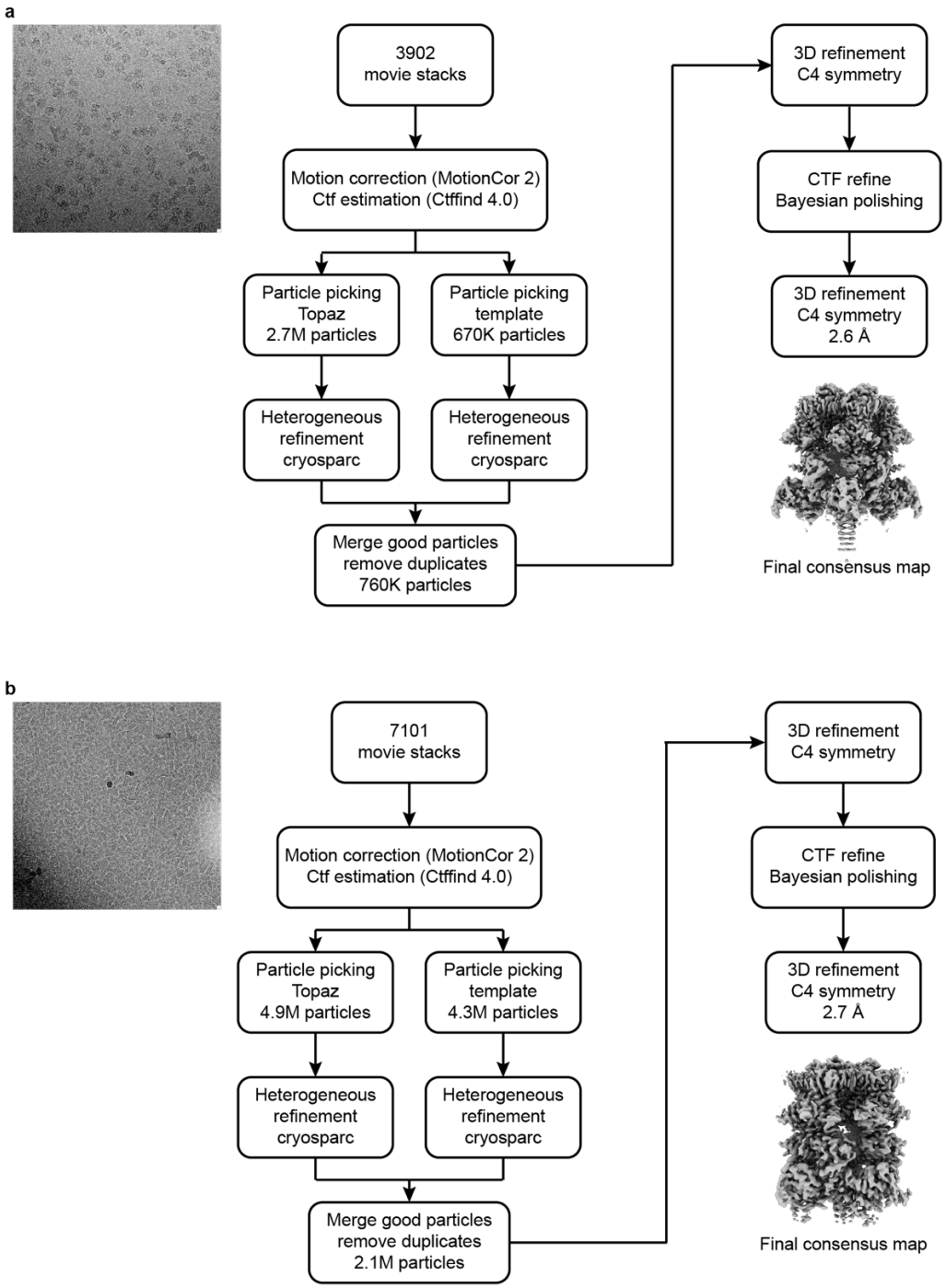

Extended Data Figure 5. Cryo-EM data processing workflow for the Ca^{2+}/TPPO–TRPM4–18 °C (a) and EGTA/TPPO–TRPM4–37 °C (b) datasets. Representative micrographs are shown. The final maps are displayed with their respective resolutions.

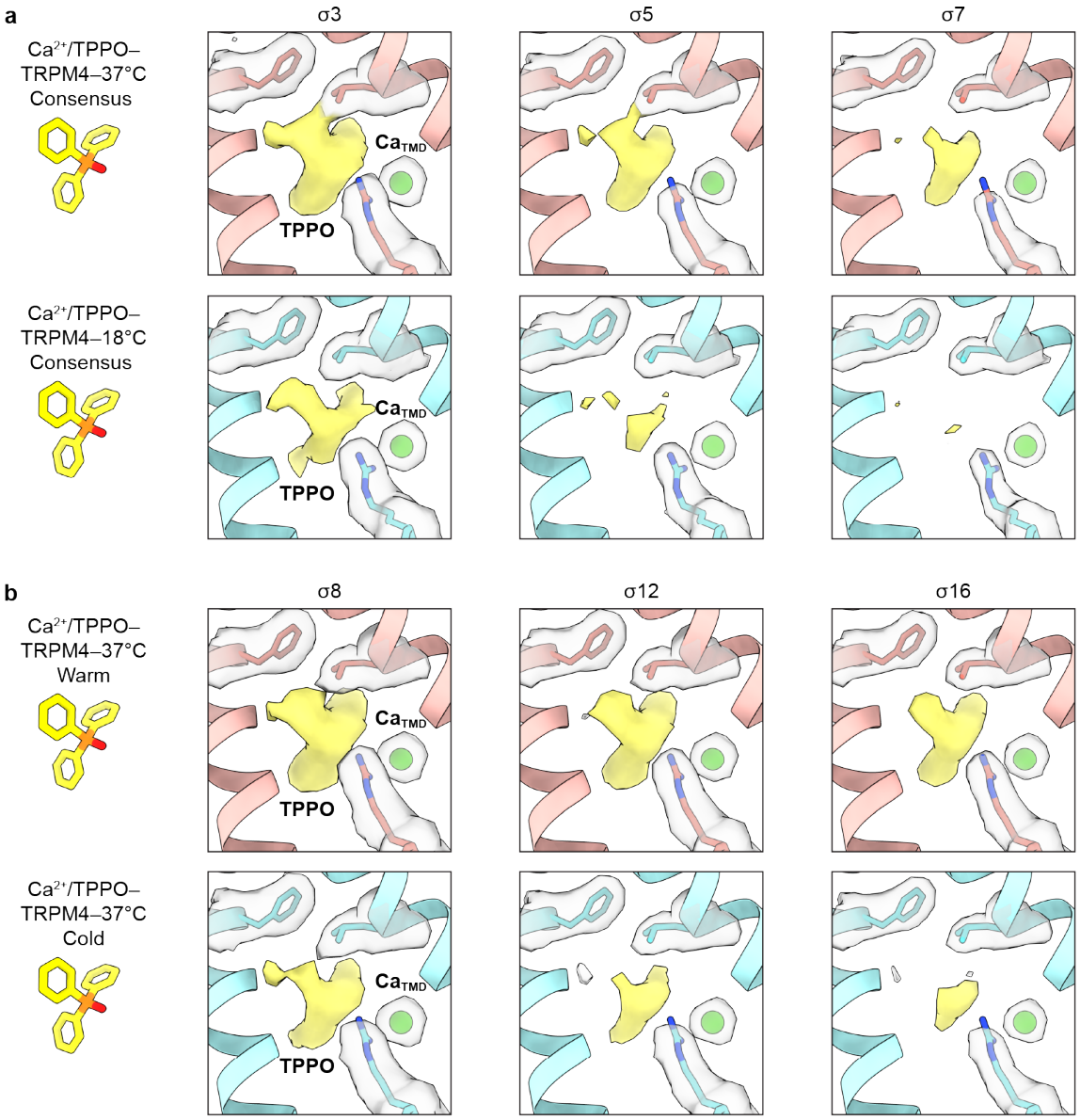

Extended Data Figure 6. Densities of the TPPO binding site from various datasets or conformations contoured at different σ levels.

Densities at the TPPO binding site are shown as yellow surfaces. For comparison, densities for Ca_{TMD} and surrounding interacting residues are displayed as transparent surfaces. The TPPO molecule in the pose fitted to the Ca^{2+}/TPPO–TRPM4–37 °C warm map is shown on the left in stick representation.

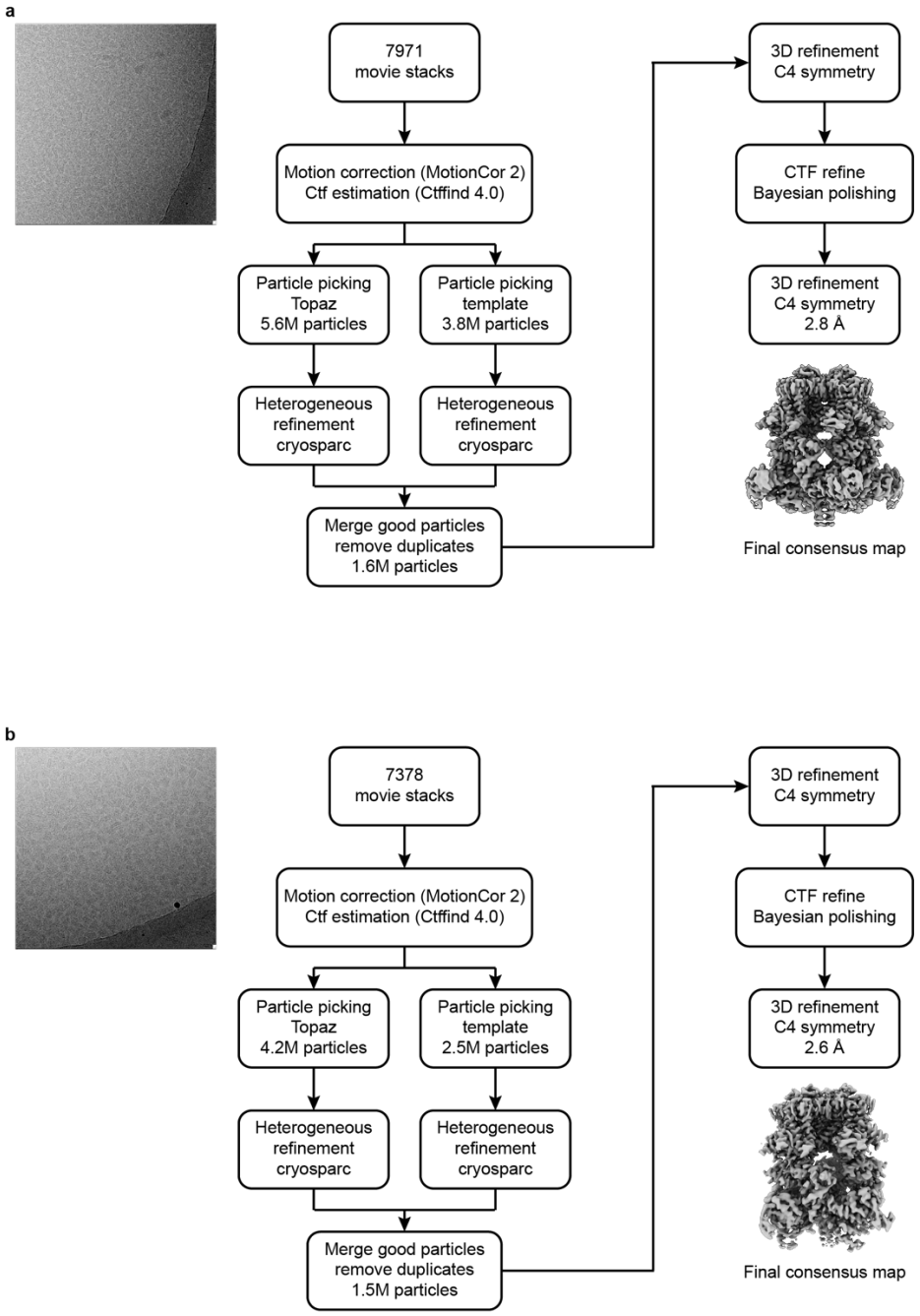

Extended Data Figure 7. Cryo-EM data processing workflow for the Ca^{2+}/NC1–TRPM4–37 °C (a) and EGTA/NC1–TRPM4–18 °C (b) datasets. Representative micrographs are shown. The final maps are displayed with their respective resolutions.

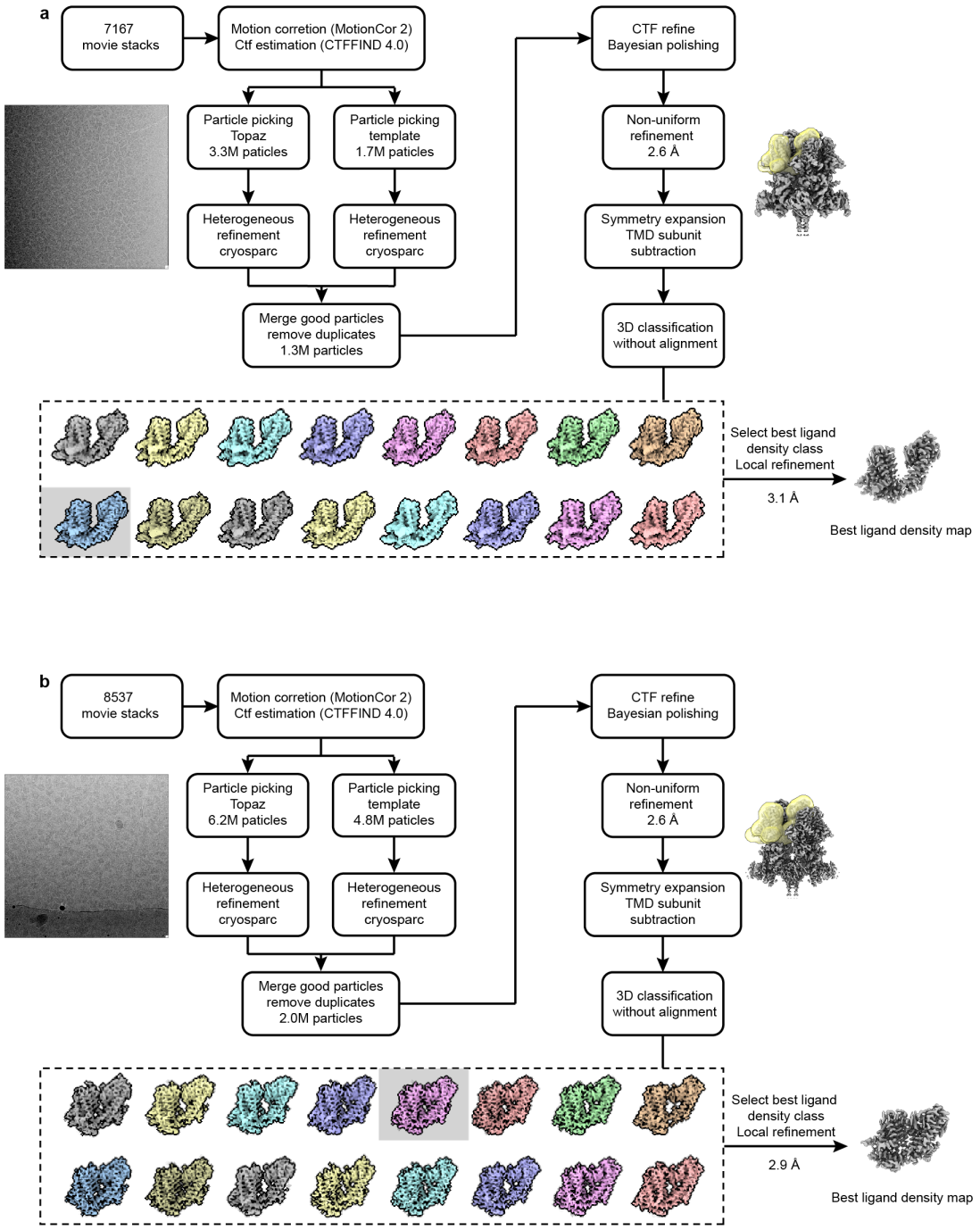

Extended Data Figure 8. Cryo-EM data processing workflow for the Ca^{2+}/CBA–TRPM4–18 °C (a) and Ca^{2+}/CBA–TRPM4–37 °C (b) datasets. Representative micrographs are shown. The final consensus map and the TMD-focused map with the best-resolved ligand density are displayed with their respective resolutions.

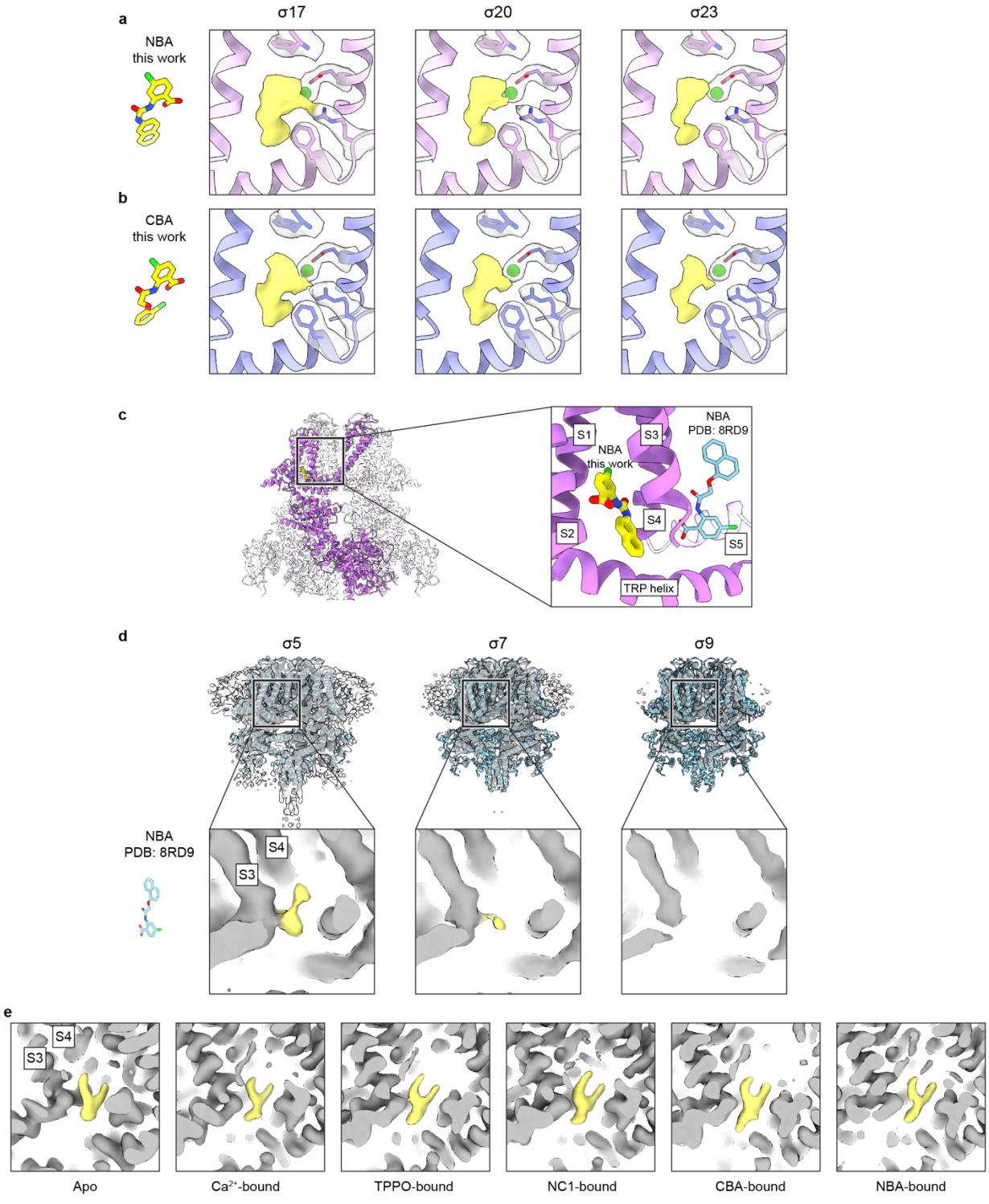

Extended Data Figure 9. Comparison of the NBA and CBA sites identified in this study with the previously reported NBA site, along with the densities observed within these sites.

741 **a**,**b**, NBA and CBA densities contoured at different σ levels for the Ca^{2+}/NBA–TRPM4–37 °C
742 TMD map and the Ca^{2+}/CBA–TRPM4–37 °C TMD map in this study. Densities of NBA and
743 CBA are shown as yellow surfaces. For comparison, densities for Ca_{TMD} and surrounding
744 interacting residues are displayed as transparent surfaces. The NBA and CBA molecules in the
745 poses fitted to the maps are shown on the left in stick representation. **c**, Location of the NBA
746 binding site identified in this work (yellow; PDB-ID 9Z24) compared with the previously
747 reported site (light blue; PDB-ID 8RD9). **d**, The overall cryo-EM map (top) and the densities of
748 the putative NBA binding site (bottom) from the previously published TRPM4 structure in the
749 presence of NBA (EMD-19069), contoured at different σ levels. The putative NBA densities are
750 highlighted in yellow, and the protein densities are shown in gray. The NBA molecule in the pose
751 fitted to the map is shown on the left in stick representation. **e**, Densities at the previously
752 reported NBA binding site in our high-resolution cryo-EM maps across different ligand
753 conditions consistently reveal a Y-shaped density characteristic of a lipid molecule. The Y-shaped
754 densities are highlighted in yellow, and the protein densities are shown in gray.

755

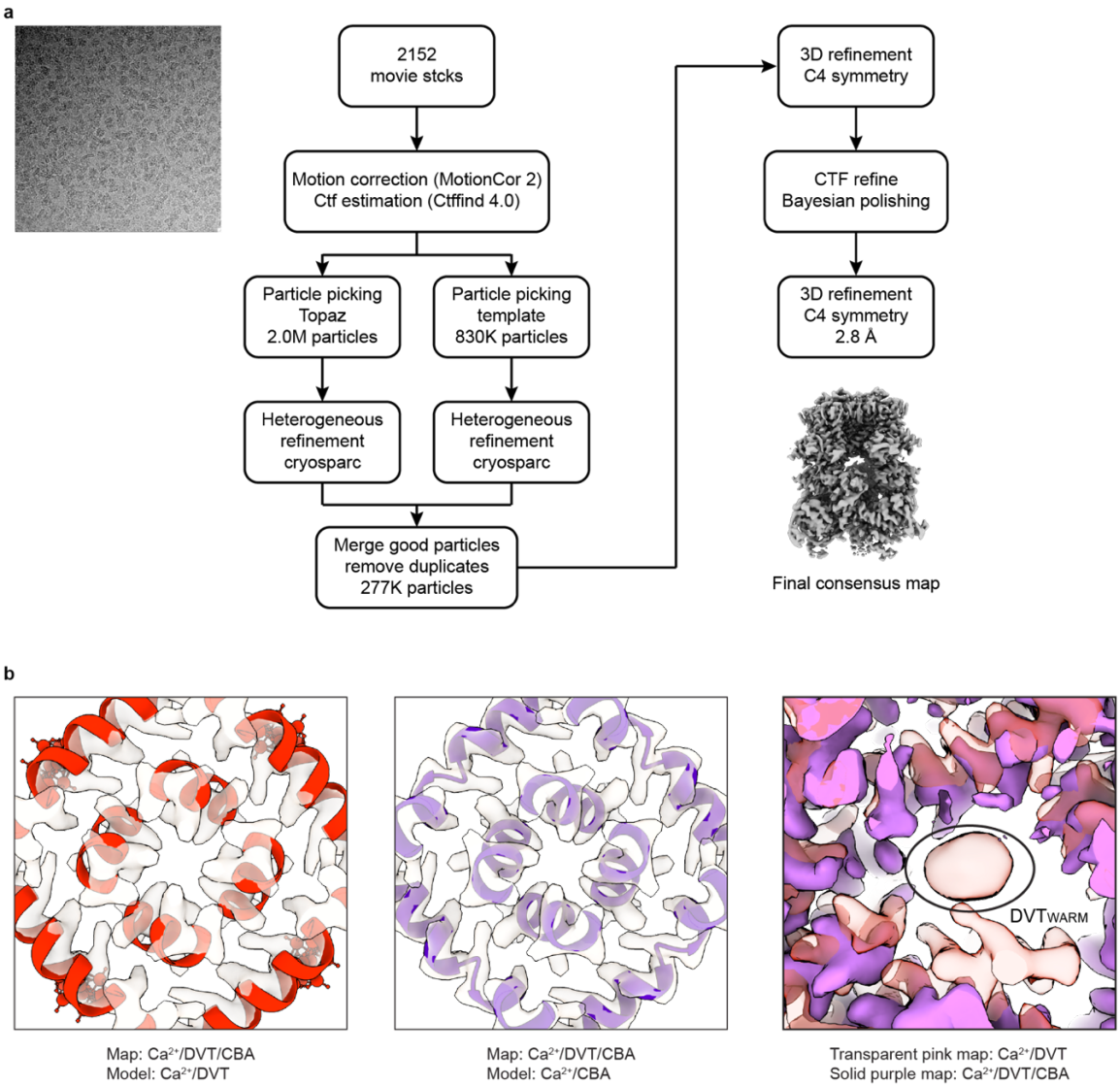

Extended Data Figure 10. Cryo-EM data processing workflow for the Ca^{2+}/DVT/CBA–TRPM4–18 °C dataset. a, A representative micrograph is shown. The final map is displayed with the resolution. **b**, Left: superimposition of the Ca^{2+}/DVT/CBA–TRPM4 map and the Ca^{2+}/DVT–TRPM4$_{Warm}$ model (red; open state), focusing on the transmembrane domain, viewed from the intracellular side. Middle: Superimposition of the Ca^{2+}/DVT/CBA–TRPM4 map and the Ca^{2+}/CBA–TRPM4 model (purple), focusing on the transmembrane domain, viewed from the intracellular side. Right: superimposition of the cryo-EM maps of Ca^{2+}/DVT/–TRPM4$_{Warm}$ (transparent pink) and Ca^{2+}/DVT/CBA–TRPM4 (solid purple), focusing on the DVT$_{Warm}$ site and its surroundings.

	Ca^{2+}/TPPO–TRPM4–37°C (EMDB-73754) (PDB 9Z1W)	Ca^{2+}/TPPO–TRPM4–37°C warm TMD (EMDB-73755) (PDB 9Z1X)	Ca^{2+}/TPPO–TRPM4–37°C cold TMD (EMDB-73756) (PDB 9Z1Y)	Ca^{2+}/TPPO–TRPM4–18°C (EMDB-73757) (PDB 9Z1Z)	EGTA/TPPO–TRPM4–37°C (EMDB-73758) (PDB 9Z20)
Data collection and processing					
Magnification	135000	135000	135000	135000	135000
Voltage (kV)	200	200	200	200	200
Electron exposure (e–/Å^2)	40	40	40	40	40
Defocus range (μm)	-0.5 – -1.4	-0.5 – -1.4	-0.5 – -1.4	-0.5 – -1.4	-0.5 – -1.4
Pixel size (Å)	0.87	0.87	0.87	0.87	0.874
Symmetry imposed	C4	C1	C1	C1	C4
Initial particle images (no.)	2.6M			2.7M	4.9M
Final particle images (no.)	1180K	882K	294K	760K	1929K
Map resolution (Å)	2.9	3.0	3.3	2.6	2.5
FSC threshold	0.143	0.143	0.143	0.143	0.143
Map resolution range (Å)	2.9 – 246.2	3.0 – 246.2	3.2 – 246.2	2.6 – 246.2	2.5 – 246.2
Refinement					
Initial model used (PDB code)	5WP6	5WP6	5WP6	5WP6	5WP6
Model resolution (Å)	3.3	3.3	3.5	3.1	2.7
FSC threshold	0.5	0.5	0.5	0.5	0.5
Model resolution range (Å)	3.3 – 246.2	3.3 – 246.2	3.5 – 246.2	3.1 – 246.2	2.7 – 246.2
Map sharpening *B* factor (Å^2)	-120	-30	-30	-100	-100
Model composition					
Non-hydrogen atoms	30220	2912	2912	29272	29312
Protein residues	3976	365	365	3892	3896
Ligands	12	2	2	12	0
B factors (Å^2)					
Protein	133.28	83.39	82.41	123.92	103.06
Ligand	144.31	98.78	95.88	78.23	
R.m.s. deviations					
Bond lengths (Å)	0.004	0.003	0.002	0.006	0.003
Bond angles (°)	0.469	0.448	0.419	0.493	0.452
Validation					
MolProbity score	1.21	1.13	1.10	1.14	0.92
Clashscore	1.89	2.41	2.24	1.69	0.97
Poor rotamers (%)	0.68	0	0	0.5	1.13
Ramachandran plot					
Favored (%)	96.15	97.49	97.49	96.63	97.58
Allowed (%)	3.85	2.51	2.51	3.37	2.42
Disallowed (%)	0	0	0	0	0

Supplementary Table 1: Cryo-EM data collection, refinement and validation statistics. Data are shown for Ca^{2+}/TPPO–TRPM4–37°C, Ca^{2+}/TPPO–TRPM4–37°C warm TMD, Ca^{2+}/TPPO–TRPM4–37°C cold TMD, Ca^{2+}/TPPO–TRPM4–18°C, and EGTA/TPPO–TRPM4–37°C.

	Ca^{2+}/NC1–TRPM4–37°C (EMDB-73759) (PDB 9Z21)	EGTA/NC1–TRPM4–37°C (EMDB-73760) (PDB 9Z22)	Ca^{2+}/CBA–TRPM4–37°C (EMDB-73761) (PDB 9Z23)	Ca^{2+}/CBA–TRPM4–37°C TMD (EMDB-73762) (PDB 9Z24)	Ca^{2+}/NBA–TRPM4–37°C (EMDB-73763) (PDB 9Z25)
Data collection and processing					
Magnification	135000	135000	135000	135000	135000
Voltage (kV)	200	200	200	200	200
Electron exposure (e–/Å^2)	40	40	40	40	40
Defocus range (μm)	-0.5 – -1.4	-0.5 – -1.4	-0.5 – -1.4	-0.5 – -1.4	-0.5 – -1.4
Pixel size (Å)	0.874	0.87	0.87	0.87	0.874
Symmetry imposed	C4	C4	C4	C1	C4
Initial particle images (no.)	5.6M	4.2M	3.3M		6.2M
Final particle images (no.)	1636K	1475K	1290K	160K	2049K
Map resolution (Å)	2.8	2.6	2.6	3.1	2.6
FSC threshold	0.143	0.143	0.143	0.143	0.143
Map resolution range (Å)	2.8 – 246.2	2.6 – 246.2	2.6 – 246.2	3.1 – 246.2	2.6 – 246.2
Refinement					
Initial model used (PDB code)	5WP6	5WP6	5WP6	5WP6	5WP6
Model resolution (Å)	3.1	2.9	3.2	3.3	2.9
FSC threshold	0.5	0.5	0.5	0.5	0.5
Model resolution range (Å)	3.1 – 246.2	2.9 – 246.2	3.2 – 246.2	3.3 – 246.2	2.9 – 246.2
Map sharpening *B* factor (Å^2)	-117	-105	-102	-50	-106
Model composition					
Non-hydrogen atoms	30300	29396	30304	2740	30300
Protein residues	3976	3900	3972	338	3972
Ligands	12	4	12	2	12
B factors (Å^2)					
Protein	107.36	100.17	108.2	101.63	114.79
Ligand	117.04	83.25	66.02	116.92	82.15
R.m.s. deviations					
Bond lengths (Å)	0.004	0.004	0.004	0.004	0.003
Bond angles (°)	0.488	0.439	0.460	0.468	0.440
Validation					
MolProbity score	1.36	1.44	1.22	1.2	1.34
Clashscore	2.14	4.57	1.6	2.19	2.35
Poor rotamers (%)	0.27	0.14	1.08	0.35	0.27
Ramachandran plot					
Favored (%)	94.62	96.74	95.79	96.69	95.28
Allowed (%)	5.38	3.26	4.21	3.31	4.72
Disallowed (%)	0	0	0	0	0

Supplementary Table 2: Cryo-EM data collection, refinement and validation statistics. Data are shown for Ca^{2+}/NC1–TRPM4–37°C, EGTA/NC1–TRPM4–37°C, Ca^{2+}/CBA–TRPM4–37°C, and Ca^{2+}/NBA–TRPM4–37°C.

	Ca^{2+}/NBA–TRPM4–37°C TMD (EMDB-73764) (PDB 9Z26)	Ca^{2+}/CBA/DVT–TRPM4–37°C (EMDB-73765) (PDB 9Z27)
Data collection and processing		
Magnification	135000	135000
Voltage (kV)	200	200
Electron exposure (e–/Å^2)	40	40
Defocus range (μm)	-0.5 – -1.4	-0.5 – -1.4
Pixel size (Å)	0.874	0.87
Symmetry imposed	C1	C4
Initial particle images (no.)		2M
Final particle images (no.)	239K	278K
Map resolution (Å)	2.9	2.8
FSC threshold	0.143	0.143
Map resolution range (Å)	2.9 – 246.2	3.8 – 246.2
Refinement		
Initial model used (PDB code)	5WP6	5WP6
Model resolution (Å)	3.2	3.2
FSC threshold	0.5	0.5
Model resolution range (Å)	3.2 – 246.2	3.2 – 246.2
Map sharpening *B* factor (Å^2)	-50	-95
Model composition		
Non-hydrogen atoms	2945	30292
Protein residues	364	3972
Ligands	2	12
B factors (Å^2)		
Protein	110.32	191.28
Ligand	125.37	118.86
R.m.s. deviations		
Bond lengths (Å)	0.004	0.002
Bond angles (°)	0.499	0.466
Validation		
MolProbity score	1.11	1.34
Clashscore	2.72	3.37
Poor rotamers (%)	0.97	0.54
Ramachandran plot		
Favored (%)	97.77	96.64
Allowed (%)	2.23	3.36
Disallowed (%)	0	0

Supplementary Table 3: Cryo-EM data collection, refinement and validation statistics. Data are shown for Ca^{2+}/NBA–TRPM4–37°C TMD, and Ca^{2+}/DVT/CBA–TRPM4–37°C.

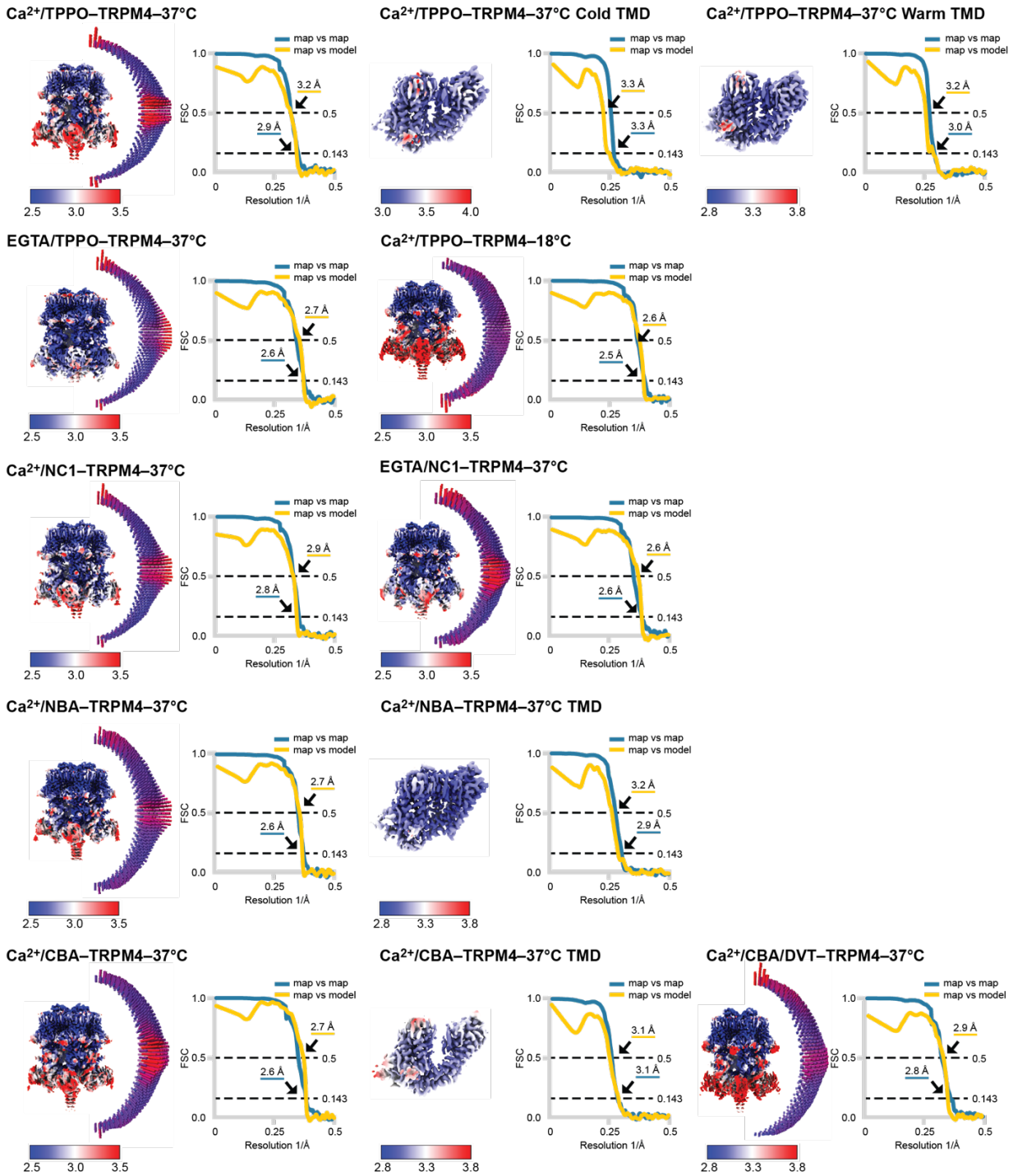

Supplementary Figure 1. Assessment of cryo-EM data quality. For each map, left: cryo-EM maps colored by local resolution; right: Fourier shell correlation (FSC) plot.

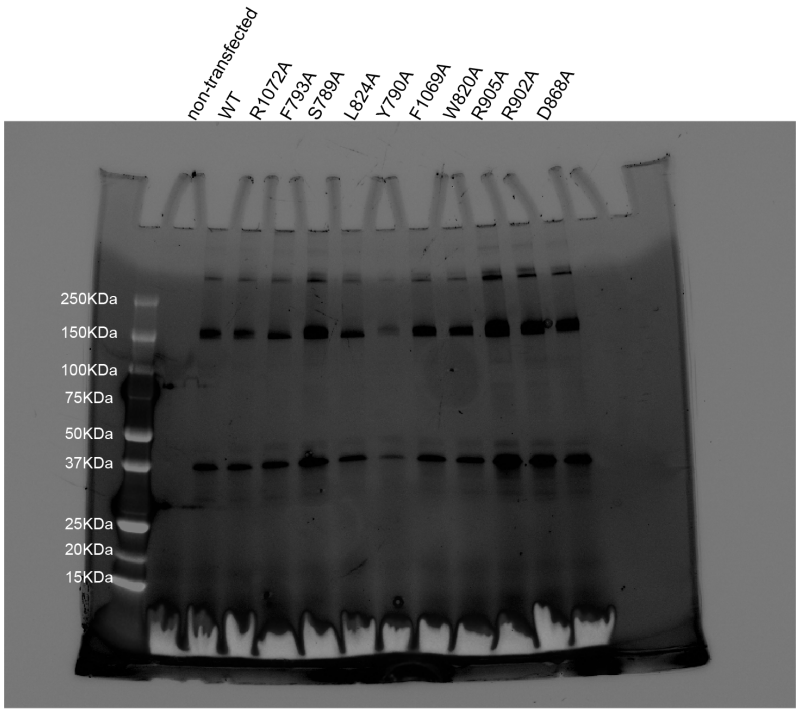

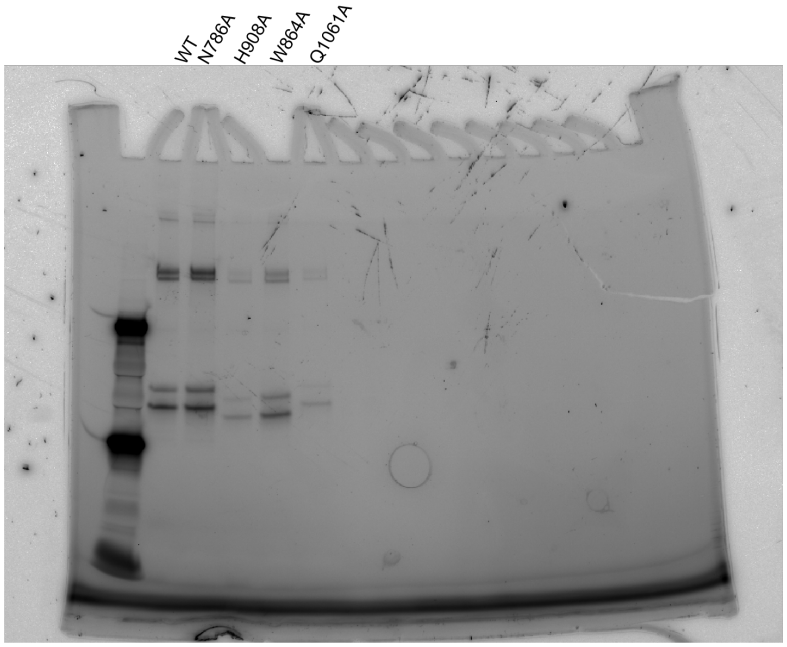

Supplementary Figure 2. In-gel fluorescence analysis of cell-surface expression of wild-type and mutant TRPM4 and following a cell-surface biotinylation assay. Bands slightly above 150 kDa correspond to GFP-tagged TRPM4, whereas bands at ~35 kDa represent free GFP.

Data Availability

Cryo-EM density maps have been deposited at the EMDB (Electron Microscopy Data Bank) and the Research Collaboratory for Structural Bioinformatics Protein Data Bank (RCS-PDB), respectively.

Acknowledgements

We thank for the support with data collection at the Structural Biology Facility at Northwestern University. We appreciate the Structural Biology Facility and Northwestern IT Research Computing and Data Services for computational support. W.L. is supported by National Institutes of Health (NIH) grants (R01HL153219 and R01NS112363, and R35GM138321). J.D. is supported by a McKnight Scholar Award, a Klingenstein-Simon Scholar Award, a Sloan Research Fellowship in neuroscience, a Pew Scholar in the Biomedical Sciences award, and NIH grants (R01NS111031 and R01NS129804). J.H. is supported by American Heart Association postdoctoral fellowship (24POST1196982). A portion of this research was supported by NIH grant R24GM154185 and performed at the Pacific Northwest Center for Cryo-EM (PNCC) with assistance from Marcelo de Farias.

Author Contributions

J.D. and W.L. supervised the project. J.H. carried out mutagenesis, protein purification, cryo-EM data collection and processing, and structural analysis for all TRPM4 structures included in the study. S.I. and J.C. contributed to the initial cryo-EM studies of TRPM4 in complex with NBA, CBA, and NC1. S.P. and J.L. performed functional experiments. G.O. and J.S. carried out mutagenesis and expression test. J.H., J.D. and W.L. wrote the manuscript, with contributions from S.P. and J.L. All authors participated in manuscript preparation and approved the final version. The authors declare no conflicts of interest.

Methods

Human TRPM4 protein expression and purification

The gene encoding human full-length TRPM4 (UniProtKB: Q8TD43) was subcloned into pEG BacMam vector with a 2×Strep tag, GFP and a thrombin-cleavage site at the N terminus[57]. Bacmid and baculovirus of TRPM4 in a BacMam vector were generated, and P2 viruses were used to infect a suspension of tsA cells. Cells were incubated at 37 °C for 8 h and10 mM sodium butyrate was added to the culture and the temperature was changed to 30 °C. The cells were collected 72 h after infection and resuspended in a buffer containing 100 mM Tris pH 8.0 and 150 mM NaCl (TBS buffer) in the presence of 1 mM phenylmethylsulphonyl fluoride, 0.8 μM aprotinin, 2 μg ml^{-1} leupeptin and 2 mM pepstatin A. The cells were lysed by sonication and the membrane fraction was collected by centrifugation at 186,000*g* using a 45 Ti rotor (Beckman Coulter) for 1 h at 4 °C. The membrane then homogenized with a Dounce homogenizer in TBS buffer supplemented with protease inhibitors. The protein was extracted from the membrane with TBS buffer supplemented with 1% GDN and protease inhibitors for 3 h at 4 °C. The solubilized proteins were loaded to Strep-Tactin resin. After washing with TBS buffer supplemented with 0.02% GDN, TRPM4 was eluted with the same buffer, supplemented with 10 mM desthiobiotin. The GFP tag were cleaved, and proteins were concentrated and further purified by size-exclusion chromatography (Superose 6). The peak fractions containing the TRPM4 were pooled and concentrated to 8 mg ml^{-1}.

EM sample preparation and data acquisition

Purified TRPM4 was incubated with 5 mM calcium chloride or 5 mM EGTA, as required for each experiment, for 30 s at 18 or 37 °C. Then 0.1mM TPPO, 0.25mM CBA/NBA or 0.8mM NC1 was added and further incubation for 2 min at 18 or 37 °C respectively. 2.5 μl sample was applied to a glow-discharged Quantifoil holey carbon grid (gold, 2/1 μm size/hole space, 300 mesh). The grids were blotted for 1.5 s in the Vitrobot Mark III set to 100% humidity and 37 °C with a 15 s wait time before being plunge-frozen into liquid ethane cooled by liquid nitrogen.

For the all the sample, images were recorded using the FEI Glacios electron microscope at 200 kV and a nominal magnification of 135,000×. A Falcon 4i direct electron detector with

840 Selectris energy filter was used resulting a pixel size of 0.87 Å or 0.874 Å. EPU was used for
841 automated acquisition. Nominal defocus ranged from −0.5 to −1.4 μm.

842 **Cryo-electron microscopy data analysis procedure**

843 The detailed workflow for the data-processing procedure is summarized in Extended Data
844 Figs. 4–5, 8, 9, 11. In general, the raw movies for each dataset were motion-corrected using
845 MotionCor2 (v.1.1.0)[58]. The per-micrograph defocus values were estimated using ctffind
846 (v.4.1.10)[59]. Particle picking was performed using relion template picker[60] and topaz (v.0.2.4)[61].
847 Junk particles were removed by rounds of 3D heterogeneous refinement using CryoSPARC[62].
848 Good particles were selected for non-uniformed refinement with C_4 symmetry in CryoSPARC to
849 generate a 3D map. Multiple rounds of CTF refinement and Bayesian polishing were performed
850 in RELION and CryoSPARC to further improve the map resolution.

851 For 37 °C with Ca^{2+} and TPPO dataset, symmetry expansion at the single subunit of ICD level
852 was done from the map refined with C_4 symmetry, followed by monomer ICD subtraction. The
853 subtracted images of the monomer ICD underwent 3D classification without image alignment in
854 RELION to identify the warm and cold conformation. The correspond warm and cold monomer
855 were subsequently undergone similar TMD monomer 3D classification to identify the best the
856 local resolution map with the bound ligand.

857 For the rest of 37 °C with Ca^{2+} dataset, symmetry expansion at the single subunit of TMD level
858 was done from the map refined with C_4 symmetry, followed by monomer TMD subtraction. The
859 subtracted images of the monomer TMD underwent 3D classification without image alignment
860 in RELION to identify the class with the best local resolution map with the bound ligand.

861 Map resolution estimates were based on the gold standard Fourier shell correlation 0.143
862 criterion for all datasets.

863 **Model building**

864 Atomic models were generated by rigid-body fitting of the TMD, MHR1/2 and MHR3/4 and C-
865 terminal domains from a published human TRPM4 model (PDB: 5WP6) into the final cryo-EM
866 maps. Ligands were fitted into the density through real-space refinement using COOT[63]. The CIF
867 file of ligands was generated using grade web server (Global Phasing Ltd.). The models were

then manually adjusted in COOT and subjected to phenix.real_space_refine[64] to improve the model metrics. The final models were validated using phenix.molprobity[65]. Figures were generated using UCSF ChimeraX[66].

Electrophysiology

TsA201 cells expressing plasmids encoding N-terminal GFP-tagged human TRPM4 WT and mutants were used. One day after transfection with plasmid DNA (100 ng ml^{-1}) and Lipofectamine 2000 (Invitrogen, 11668019), the cells were trypsinized and replated onto poly-L-lysine-coated (Sigma, P4707) glass coverslips. After cell attachment, the coverslip was transferred to a recording chamber. Whole-cell patch-clamp recordings were performed at room temperature (21–23 °C) or body temperature (36–38 °C). The temperature of perfusion solutions was controlled by thermal control devices (SC-20/CL-100, Warner Instruments).

For whole-cell recordings, glass pipettes were pulled to 3–5 MΩ and filled with an internal solution. Signals were amplified with a MultiClamp 700B amplifier (controlled by MultiClamp Commander v2.2.2.2) and digitized using a Digidata 1550B A/D converter controlled by Clampex v11.3 (Molecular Devices). Whole-cell currents were measured in cells with an access resistance of < 10 MΩ after achieving whole-cell configuration. Whole-cell capacitance was compensated by the amplifier circuitry. Whole-cell currents were recorded using a two-step voltage protocol in which cells were held at –100 mV for 200 ms and then stepped to +100 mV for another 200 ms, repeated every 10 s. An alternative voltage-step protocol was applied, in which cells were stepped from –100 mV to +140 mV in 20-mV increments, with each step lasting 100 ms. A voltage ramp from –100 to +100 mV (200 ms duration) was applied every 5 s from a holding potential of 0 mV. Data were sampled at 10 kHz and low-pass filtered at 2 kHz. Recordings were analyzed using Clampfit v11.3 (Axon Instruments), GraphPad Prism v10.6.1 (GraphPad Software, Inc., La Jolla, CA), and OriginPro 2024 (OriginLab, Northampton, MA). Data were also analyzed using custom Python scripts, including pyABF for loading and processing ABF electrophysiology files. Electrophysiology files were parsed and analyzed in Python v3.11.8 executed in Spyder v6.0.7 (Anaconda environment) on macOS v26.0.1 (ARM architecture). Data processing used pandas v2.2.2 and numerical operations used NumPy v1.26.4. All custom analysis scripts used in this study are available at https://github.com/junuk861/ephys-analysis-scripts. The bath solution (pH 7.4) contained 150

898 mM NaCl, 3 mM KCl, 10 mM HEPES, 2 mM $CaCl_2$, 1 mM $MgCl_2$, and 12 mM mannitol. Patch
899 pipettes were filled with internal solutions containing 150 mM NaCl, 1 mM $MgCl_2$, 10 mM
900 HEPES, 5 mM EGTA, and $CaCl_2$ adjusted (0 or 1.69 mM) to yield 0 or 0.1 μM free Ca^{2+},
901 respectively (pH 7.3,
902 22 °C) (source: https://somapp.ucdmc.ucdavis.edu/pharmacology/bers/maxchelator/CaEGTA-
903 TS.htm). For whole-cell recordings of NC1-induced and NBA/CBA-inhibited currents, the
904 extracellular solution contained the following (in mM): 150 NaCl, 10 HEPES and 1 $MgCl_2$. The
905 intracellular solution contained (in mM): 150 NaCl, 10 HEPES and 5 EGTA. The intracellular
906 concentration of $CaCl_2$ was set to either 0, 1.69 or 4.45 mM (corresponding to 0, 0.1 or 1 μM of
907 free Ca^{2+}). The pH was adjusted to 7.4 using NaOH in both the extracellular and intracellular
908 solutions.

909 TPPO (Sigma-Aldrich, T84603) was prepared daily as a 70 mM stock solution in ethanol and
910 diluted to the desired final concentration in the bath solution immediately before use. NC1
911 (Necrocide 1, MCE, HY-14307), NBA (4-chloro-2-(2-(naphthalen-1-yloxy)acetamido)benzoic
912 acid, MCE, HY-128172), and CBA (4-chloro-2-[2-(2-chloro-phenoxy)-acetylamino]-benzoic
913 acid, Tocris, 6724) were dissolved in DMSO to a stock concentration of 10, 100, and 50 mM,
914 respectively.

915 **Surface protein labeling**

916 Surface protein labeling experiments were performed using the Pierce™ Cell Surface Protein
917 Isolation Kit (Thermo Fisher Scientific). Surface and total protein levels of wild-type and mutant
918 TRPM4 were assessed by in-gel fluorescence of the N-terminal GFP tag.

919

920 **References**

921 1 Gao, Y., Cao, E., Julius, D. & Cheng, Y. TRPV1 structures in nanodiscs reveal
922 mechanisms of ligand and lipid action. *Nature* **534**, 347-351 (2016).
923 https://doi.org/10.1038/nature17964
924 2 Yang, X. *et al*. Structure deformation and curvature sensing of PIEZO1 in lipid
925 membranes. *Nature* **604**, 377-383 (2022). https://doi.org/10.1038/s41586-022-
926 04574-8

927 3 Yao, X., Fan, X. & Yan, N. Cryo-EM analysis of a membrane protein embedded in the
928 liposome. *Proc Natl Acad Sci U S A* **117**, 18497-18503 (2020).
929 https://doi.org/10.1073/pnas.2009385117
930 4 Tao, X., Zhao, C. & MacKinnon, R. Membrane protein isolation and structure
931 determination in cell-derived membrane vesicles. *Proc Natl Acad Sci U S A* **120**,
932 e2302325120 (2023). https://doi.org/10.1073/pnas.2302325120
933 5 Zhou, J. *et al.* Resolving native GABA(A) receptor structures from the human brain.
934 *Nature* **638**, 562-568 (2025). https://doi.org/10.1038/s41586-024-08454-1
935 6 Lin, S., Ke, M., Zhang, Y., Yan, Z. & Wu, J. Structure of a mammalian sperm cation
936 channel complex. *Nature* **595**, 746-750 (2021). https://doi.org/10.1038/s41586-021-
937 03742-6
938 7 Zhang, M. *et al.* Assembly and architecture of endogenous NMDA receptors in adult
939 cerebral cortex and hippocampus. *Cell* **188**, 1198-1207 e1113 (2025).
940 https://doi.org/10.1016/j.cell.2025.01.004
941 8 Jeong, H. *et al.* Structures of the TMC-1 complex illuminate mechanosensory
942 transduction. *Nature* **610**, 796-803 (2022). https://doi.org/10.1038/s41586-022-
943 05314-8
944 9 Kumar Mondal, A., Carrillo, E., Jayaraman, V. & Twomey, E. C. Glutamate gating of
945 AMPA-subtype iGluRs at physiological temperatures. *Nature* (2025).
946 https://doi.org/10.1038/s41586-025-08770-0
947 10 Hu, J. *et al.* Physiological temperature drives TRPM4 ligand recognition and gating.
948 *Nature* **630**, 509-515 (2024). https://doi.org/10.1038/s41586-024-07436-7
949 11 Bootman, M. D. & Bultynck, G. Fundamentals of Cellular Calcium Signaling: A
950 Primer. *Cold Spring Harb Perspect Biol* **12** (2020).
951 https://doi.org/10.1101/cshperspect.a038802
952 12 Zhang, W. H. *et al.* Association of concomitant H1 antihistamine and immune
953 checkpoint inhibitor therapy on survival outcome and safety in patients with
954 advanced primary lung cancer: a cohort study. *Transl Lung Cancer Res* **13**, 2787-
955 2801 (2024). https://doi.org/10.21037/tlcr-24-795
956 13 Launay, P. *et al.* TRPM4 is a Ca2+-activated nonselective cation channel mediating
957 cell membrane depolarization. *Cell* **109**, 397-407 (2002).
958 https://doi.org/10.1016/s0092-8674(02)00719-5
959 14 Nilius, B. *et al.* Voltage dependence of the Ca2+-activated cation channel TRPM4. *J*
960 *Biol Chem* **278**, 30813-30820 (2003). https://doi.org/10.1074/jbc.M305127200
961 15 Talavera, K. *et al.* Heat activation of TRPM5 underlies thermal sensitivity of sweet
962 taste. *Nature* **438**, 1022-1025 (2005). https://doi.org/10.1038/nature04248
963 16 Cheng, H. *et al.* TRPM4 controls insulin secretion in pancreatic beta-cells. *Cell*
964 *Calcium* **41**, 51-61 (2007). https://doi.org/10.1016/j.ceca.2006.04.032
965 17 Pironet, A., Vandewiele, F. & Vennekens, R. Exploring the role of TRPM4 in calcium-
966 dependent triggered activity and cardiac arrhythmias. *J Physiol* **602**, 1605-1621
967 (2024). https://doi.org/10.1113/JP283831
968 18 Vandewiele, F. *et al.* TRPM4 inhibition by meclofenamate suppresses Ca2+-
969 dependent triggered arrhythmias. *Eur Heart J* **43**, 4195-4207 (2022).
970 https://doi.org/10.1093/eurheartj/ehac354

19 Yan, J., Bengtson, C. P., Buchthal, B., Hagenston, A. M. & Bading, H. Coupling of NMDA receptors and TRPM4 guides discovery of unconventional neuroprotectants. *Science* **370** (2020). https://doi.org/10.1126/science.aay3302

20 Menigoz, A. *et al.* TRPM4-dependent post-synaptic depolarization is essential for the induction of NMDA receptor-dependent LTP in CA1 hippocampal neurons. *Pflugers Arch* **468**, 593-607 (2016). https://doi.org/10.1007/s00424-015-1764-7

21 Schattling, B. *et al.* TRPM4 cation channel mediates axonal and neuronal degeneration in experimental autoimmune encephalomyelitis and multiple sclerosis. *Nat Med* **18**, 1805-1811 (2012). https://doi.org/10.1038/nm.3015

22 Shimizu, T. *et al.* TRPM4 regulates migration of mast cells in mice. *Cell Calcium* **45**, 226-232 (2009). https://doi.org/10.1016/j.ceca.2008.10.005

23 Barbet, G. *et al.* The calcium-activated nonselective cation channel TRPM4 is essential for the migration but not the maturation of dendritic cells. *Nat Immunol* **9**, 1148-1156 (2008). https://doi.org/10.1038/ni.1648

24 Guinamard, R., Demion, M., Chatelier, A. & Bois, P. Calcium-activated nonselective cation channels in mammalian cardiomyocytes. *Trends Cardiovasc Med* **16**, 245-250 (2006). https://doi.org/10.1016/j.tcm.2006.04.007

25 Liu, Y. *et al.* Noncanonical calcium-independent TRPM4 activation governs intestinal fluid homeostasis. *Nat Commun* (2026). https://doi.org/10.1038/s41467-025-68014-7

26 Dai, Y., Wang, H., Wang, W. & Zhuang, X. Multidimensional pan cancer analysis of the sodium induced cell death gene TRPM4. *Sci Rep* **15**, 29768 (2025). https://doi.org/10.1038/s41598-025-15082-w

27 Guo, J. *et al.* TRPM4 channels contribute to Adriamycin chemoresistance in breast cancer cells. *Eur J Pharmacol* **998**, 177637 (2025). https://doi.org/10.1016/j.ejphar.2025.177637

28 Kappel, S. *et al.* TRPM4 is highly expressed in human colorectal tumor buds and contributes to proliferation, cell cycle, and invasion of colorectal cancer cells. *Mol Oncol* **13**, 2393-2405 (2019). https://doi.org/10.1002/1878-0261.12566

29 Sagredo, A. I. *et al.* TRPM4 regulates Akt/GSK3-beta activity and enhances beta-catenin signaling and cell proliferation in prostate cancer cells. *Mol Oncol* **12**, 151-165 (2018). https://doi.org/10.1002/1878-0261.12100

30 Gualandi, F. *et al.* Mutation Load of Multiple Ion Channel Gene Mutations in Brugada Syndrome. *Cardiology* **137**, 256-260 (2017). https://doi.org/10.1159/000471792

31 Saito, Y. *et al.* TRPM4 Mutation in Patients With Ventricular Noncompaction and Cardiac Conduction Disease. *Circ Genom Precis Med* **11**, e002103 (2018). https://doi.org/10.1161/CIRCGEN.118.002103

32 Hof, T. *et al.* TRPM4 non-selective cation channel variants in long QT syndrome. *BMC Med Genet* **18**, 31 (2017). https://doi.org/10.1186/s12881-017-0397-4

33 Liu, H. *et al.* Molecular genetics and functional anomalies in a series of 248 Brugada cases with 11 mutations in the TRPM4 channel. *PLoS One* **8**, e54131 (2013). https://doi.org/10.1371/journal.pone.0054131

1013 34 Liu, H. *et al.* Gain-of-function mutations in TRPM4 cause autosomal dominant
1014 isolated cardiac conduction disease. *Circ Cardiovasc Genet* **3**, 374-385 (2010).
1015 https://doi.org/10.1161/CIRCGENETICS.109.930867
1016 35 Palmer, R. K. *et al.* Triphenylphosphine oxide is a potent and selective inhibitor of the
1017 transient receptor potential melastatin-5 ion channel. *Assay Drug Dev Technol* **8**,
1018 703-713 (2010). https://doi.org/10.1089/adt.2010.0334
1019 36 Fu, W. *et al.* Persistent activation of TRPM4 triggers necrotic cell death characterized
1020 by sodium overload. *Nat Chem Biol* **21**, 1238-1249 (2025).
1021 https://doi.org/10.1038/s41589-025-01841-3
1022 37 Ozhathil, L. C. *et al.* Identification of potent and selective small molecule inhibitors
1023 of the cation channel TRPM4. *Br J Pharmacol* **175**, 2504-2519 (2018).
1024 https://doi.org/10.1111/bph.14220
1025 38 Bochen, F. *et al.* TRPM4 contributes to cell death in prostate cancer tumor
1026 spheroids, and to extravasation and metastasis in a zebrafish xenograft model
1027 system. *Mol Oncol* **19**, 1299-1309 (2025). https://doi.org/10.1002/1878-0261.13795
1028 39 Nilius, B., Prenen, J., Voets, T. & Droogmans, G. Intracellular nucleotides and
1029 polyamines inhibit the Ca2+-activated cation channel TRPM4b. *Pflugers Arch* **448**,
1030 70-75 (2004). https://doi.org/10.1007/s00424-003-1221-x
1031 40 Ekundayo, B. *et al.* Identification of a binding site for small molecule inhibitors
1032 targeting human TRPM4. *Nat Commun* **16**, 833 (2025).
1033 https://doi.org/10.1038/s41467-025-56131-2
1034 41 Cao, E., Liao, M., Cheng, Y. & Julius, D. TRPV1 structures in distinct conformations
1035 reveal activation mechanisms. *Nature* **504**, 113-118 (2013).
1036 https://doi.org/10.1038/nature12823
1037 42 Ruan, Z. *et al.* Structures of the TRPM5 channel elucidate mechanisms of activation
1038 and inhibition. *Nat Struct Mol Biol* **28**, 604-613 (2021).
1039 https://doi.org/10.1038/s41594-021-00607-4
1040 43 Guo, J. *et al.* Structures of the calcium-activated, non-selective cation channel
1041 TRPM4. *Nature* **552**, 205-209 (2017). https://doi.org/10.1038/nature24997
1042 44 Autzen, H. E. *et al.* Structure of the human TRPM4 ion channel in a lipid nanodisc.
1043 *Science* **359**, 228-232 (2018). https://doi.org/10.1126/science.aar4510
1044 45 Winkler, P. A., Huang, Y., Sun, W., Du, J. & Lu, W. Electron cryo-microscopy structure
1045 of a human TRPM4 channel. *Nature* **552**, 200-204 (2017).
1046 https://doi.org/10.1038/nature24674
1047 46 Huang, Y., Kumar, S., Lee, J., Lu, W. & Du, J. Coupling enzymatic activity and gating in
1048 an ancient TRPM chanzyme and its molecular evolution. *Nat Struct Mol Biol* **31**,
1049 1509-1521 (2024). https://doi.org/10.1038/s41594-024-01316-4
1050 47 Nilius, B., Prenen, J., Janssens, A., Voets, T. & Droogmans, G. Decavanadate
1051 modulates gating of TRPM4 cation channels. *J Physiol* **560**, 753-765 (2004).
1052 https://doi.org/10.1113/jphysiol.2004.070839
1053 48 Teixeira-Duarte, C. M., Zeng, W. & Jiang, Y. Structural landscape of activation,
1054 desensitization and inhibition in the human TRPM4 channel. *Nat Struct Mol Biol* **33**,
1055 43-52 (2026). https://doi.org/10.1038/s41594-025-01705-3

49 Yin, Y. *et al.* Molecular basis of neurosteroid and anticonvulsant regulation of TRPM3. *Nat Struct Mol Biol* **32**, 828-840 (2025). https://doi.org/10.1038/s41594-024-01463-8

50 Kumar, S. *et al.* Structural basis for agonist and heat activation of nociceptor TRPM3. *Nat Struct Mol Biol* (2025). https://doi.org/10.1038/s41594-025-01692-5

51 Ruan, Z. *et al.* A single allosteric site merges activation, modulation and inhibition in TRPM5. *Nat Chem Biol* (2026). https://doi.org/10.1038/s41589-025-02097-7

52 Diver, M. M., Cheng, Y. & Julius, D. Structural insights into TRPM8 inhibition and desensitization. *Science* **365**, 1434-1440 (2019). https://doi.org/10.1126/science.aax6672

53 Yin, Y. *et al.* Structural basis of cooling agent and lipid sensing by the cold-activated TRPM8 channel. *Science* **363** (2019). https://doi.org/10.1126/science.aav9334

54 Zhao, C. *et al.* Structures of a mammalian TRPM8 in closed state. *Nat Commun* **13**, 3113 (2022). https://doi.org/10.1038/s41467-022-30919-y

55 Stachowski, T. R. & Fischer, M. Unfreezing structural biology for drug discovery. *Nat Chem Biol* **22**, 169-179 (2026). https://doi.org/10.1038/s41589-025-02047-3

56 Tito, G., Ferraro, G. & Merlino, A. Dirhodium Tetraacetate Binding to Lysozyme at Body Temperature. *Int J Mol Sci* **26** (2025). https://doi.org/10.3390/ijms26146582

57 Goehring, A. *et al.* Screening and large-scale expression of membrane proteins in mammalian cells for structural studies. *Nat Protoc* **9**, 2574-2585 (2014). https://doi.org/10.1038/nprot.2014.173

58 Zheng, S. Q. *et al.* MotionCor2: anisotropic correction of beam-induced motion for improved cryo-electron microscopy. *Nat Methods* **14**, 331-332 (2017). https://doi.org/10.1038/nmeth.4193

59 Rohou, A. & Grigorieff, N. CTFFIND4: Fast and accurate defocus estimation from electron micrographs. *J Struct Biol* **192**, 216-221 (2015). https://doi.org/10.1016/j.jsb.2015.08.008

60 Scheres, S. H. RELION: implementation of a Bayesian approach to cryo-EM structure determination. *J Struct Biol* **180**, 519-530 (2012). https://doi.org/10.1016/j.jsb.2012.09.006

61 Bepler, T., Kelley, K., Noble, A. J. & Berger, B. Topaz-Denoise: general deep denoising models for cryoEM and cryoET. *Nat Commun* **11**, 5208 (2020). https://doi.org/10.1038/s41467-020-18952-1

62 Punjani, A., Rubinstein, J. L., Fleet, D. J. & Brubaker, M. A. cryoSPARC: algorithms for rapid unsupervised cryo-EM structure determination. *Nat Methods* **14**, 290-296 (2017). https://doi.org/10.1038/nmeth.4169

63 Emsley, P., Lohkamp, B., Scott, W. G. & Cowtan, K. Features and development of Coot. *Acta Crystallogr D Biol Crystallogr* **66**, 486-501 (2010). https://doi.org/10.1107/S0907444910007493

64 Afonine, P. V. *et al.* Real-space refinement in PHENIX for cryo-EM and crystallography. *Acta Crystallogr D Struct Biol* **74**, 531-544 (2018). https://doi.org/10.1107/S2059798318006551

65 Chen, V. B. *et al.* MolProbity: all-atom structure validation for macromolecular crystallography. *Acta Crystallogr D Biol Crystallogr* **66**, 12-21 (2010). https://doi.org/10.1107/S0907444909042073

66 Pettersen, E. F. *et al.* UCSF Chimera--a visualization system for exploratory research and analysis. *J Comput Chem* **25**, 1605-1612 (2004). https://doi.org/10.1002/jcc.20084